Title
Probing Polaritons in 2D Materials with Synchrotron Infrared Nanospectroscopy

Permalink
https://escholarship.org/uc/item/1599x73d

Journal
Advanced Optical Materials, 8(5)

ISSN
2195-1071

Authors
Barcelos, Ingrid D
Bechtel, Hans A
de Matos, Christiano JS
et al.

Publication Date
2020-03-01

DOI
10.1002/adom.201901091

Probing polaritons in two-dimensional materials with synchrotron infrared nanospectroscopy

Ingrid D. Barcelos, Hans A. Bechtel, Christiano J. S. de Matos, Dario A. Bahamon, Bernd Kaestner, Francisco C. B. Maia and Raul O. Freitas**

Dr. I. D. Barcelos, Dr. F. C. B. Maia, Dr. R. O. Freitas
Brazilian Synchrotron Light Laboratory (LNLS), Brazilian Center for Research in Energy and Materials (CNPEM), Zip Code 13083-970, Campinas, Sao Paulo, Brazil
e-mail: francisco.maia@lnls.br, raul.freitas@lnls.br

Dr. H. A. Bechtel
Advanced Light Source, Lawrence Berkeley National Laboratory, Berkeley, California 94720, USA.

Prof. C. J. S. de Matos, Prof. D. A. Bahamon
MackGraphe - Graphene and Nanomaterials Research Center, Mackenzie Presbyterian University, 01302-907, São Paulo, Brazil

Dr. B. Kaestner
Physikalisch-Technische Bundesanstalt (PTB), Abbestr. 2-12, 10587 Berlin, Germany

Keywords: infrared synchrotron nanospectroscopy, s-SNOM, far-infrared SINS, polaritons, 2D materials, graphene, hexagonal boron nitride.

Abstract

Polaritons, which are quasiparticles composed of a photon coupled to an electric or magnetic dipole, are a major focus in nanophotonic research of van der Waals (vdW) crystals and their derived two-dimensional (2D) materials. For the variety of existing vdW materials, polaritons can be active in a broad range of the electromagnetic spectrum (meVs to eVs) and exhibit momenta much higher than the corresponding free-space radiation. Hence, the use of high momentum broadband sources or probes is imperative to excite the polaritons and measure the frequency-momentum dispersion relations, which provide insights into polariton dynamics. Synchrotron Infrared Nanospectroscopy (SINS) is a technique that combines the nanoscale spatial resolution of scattering-type Scanning Near-field Optical Microscopy with ultrabroadband synchrotron infrared radiation, making it highly suitable to probe and characterize a variety of vdW polaritons. Here, we review the advances enabled by SINS on the study of key photonic attributes of far- and mid-infrared plasmon- and phonon-polaritons in vdW and 2D crystals. In that context we comprehensively describe the SINS technique and demonstrate how it can retrieve fundamental polaritonic properties of a range of atomically thin systems including hBN, MoS_2, graphene and 2D heterostructures.

1. Introduction

Polaritons are hybrid quasiparticles formed by the strong coupling between photons and resonant phenomena in matter.[1] These hybrid light-matter modes can originate from the coupling between electromagnetic waves and collective oscillations of charges (plasmon-polaritons, see Figure 1a), coherent vibration of crystal lattices (phonon-polaritons, see Figure 1b), electron-hole pairs (exciton-polaritons), loosely bound pair of electrons with opposite spins (Cooper pair-polaritons) and magnetic resonances (magnon-polaritons).[2,3] All these hybrid modes allow light confinement, as the polariton wavelength (λ_p) tends to be much smaller than the wavelength of the free-space excitation (λ_0), resulting in enhanced light-matter interaction.[3] Recently, remarkable features of subdiffractional polaritons have been observed in van der Waals (vdW) crystals[4–8] and in their corresponding two-dimensional (2D) materials.[9],[3] Most of those observations stem from real-space images of exciton-polaritons in transition metal dichalcogenides,[10–12] plasmon-polaritons in graphene,[13],[14] phonon-polaritons in polar vdW crystals[15],[16] and hybrid plasmon-phonon polaritons in vdW heterostructures.[17],[18] For these studies, the use of advanced optical methods such as scattering Scanning Near-field Optical Microscopy (s-SNOM),[19–21],[22] Synchrotron Infrared Nanospectroscopy (SINS)[23],[24],[25] and, more recently, Photo-induced Force Microscopy (PiFM)[26] have been paramount. Those nanoscopic techniques use the strongly concentrated optical fields confined at the nanometersized apex of an Atomic Force Microscopy (AFM) metallic tip, typically with radius ~25 nm, to excite and detect such polaritons. The broad distribution of momenta in these probes peaks $\sim 3\times 10^5$ cm^{-1}, corresponding to approximately the inverse of the tip radius, and matches the high momenta of a wide range of subdiffractional polaritons in 2D and vdW materials.

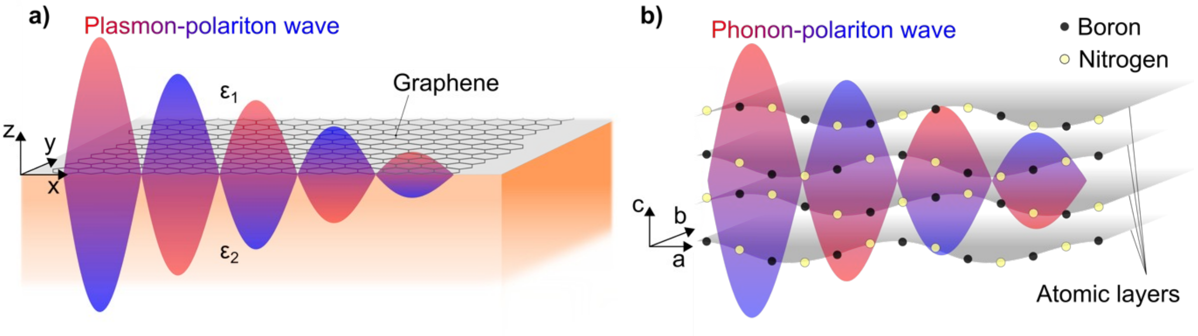

Figure 1 – Schematic illustration of the polaritonic phenomena and materials reviewed in this paper. Graphene plasmon- (a) and hBN phonon-polaritons (b) showing the electromagnetic wave coupled with the material resonances, namely collective oscillating free-electrons and optical phonons, respectively.

In particular, mid-infrared (mid-IR) plasmon- (Figure 1a) and phonon-polaritons (Figure 1b) supported by graphene and hexagonal boron nitride vdW crystals have been massively studied by s-SNOM and SINS. In general, those reports describe the dynamics of polaritons via the angular frequency[a]-momentum (ω–q) dispersion relations, from which several properties can be extracted, including the degree of light confinement and group velocity of the polariton pulse. While s-SNOM measurements typically use a series of step-tunable continuous wave lasers or optical parametric amplifiers to determine the $\omega - q$ dispersion, SINS takes advantage of the high brilliance in the mid- and far-IR of a broadband synchrotron beam to obtain the $\omega - q$ curve simultaneously, including all

---

[a] In this review, the angular frequency ω is given in units of cm^{-1}, being equal to the wavenumber. This is obtained by setting $2\pi c = 1$, as conventionally adopted in spectroscopy and in the herein reviewed works.

the bands of interest for polaritons. This review article provides an overview on how SINS is helping to unveil the behavior of such polaritons in a variety of vdW systems. A brief introduction to the physics of plasmon- and phonon-polaritons in vdW materials is presented and is accompanied by a practical procedure for extracting fundamental properties from experimental SINS data. A description of SINS is then provided. Further, reported studies using SINS are discussed, including the observation of polaritons in hexagonal boron nitride (hBN), phonon-polariton-assisted nanoimaging of local strain in hBN, mid-IR localized plasmons in individual metal-oxide nanocrystals, plasmonic phenomena in CVD-grown MoS_2 monolayers and nanophotonics of graphene-talc 2D heterostructures. Finally, we review an extreme case where the vast energy coverage of SINS is exploited: a study of graphene plasmonics in the mid-IR to far-IR continuous range (wavelengths from 5-30 µm). Despite the fast evolution of lasers for s-SNOM, the recent realization of far-IR SINS emphasizes the importance of synchrotrons as complementary sources alongside lasers.

1.1. Infrared polaritons in 2D materials

Mid-IR surface plasmons[13],[14] active in single-layered atomically thin graphene[27] are surface confined subdiffractional electromagnetic modes, named surface plasmon-polaritons (SPP). They exhibit relatively large q ($q = \frac{2\pi}{\lambda_p}$) and propagate along the material‘s surface plane (x-y) while being evanescent on the out-of-plane direction (z). In general, these modes can be described as evanescent electric and magnetic fields originated from top surface layers of the material, with conductivity σ and located in between media with different dielectric functions $\varepsilon_{1,2}$ (Figure 1a). By defining the propagation along the x direction, they can be described in the form $F(x) = F_{1,2} e^{\mp \kappa_{1,2} z} e^{iqx}$, satisfying Maxwell’s equations for $\kappa_{1,2} = \sqrt{q^2 - \frac{\varepsilon_{1,2}\,\omega^2}{c^2}}$, where 1 and 2 refer to the two adjacent media (ε_1 and ε_2, respectively, as Figure 1a). $\varepsilon_{1,2}$, $F_{1,2}$ and $\kappa_{1,2}$ are the dielectric functions, wave amplitudes and out-of-plane momenta, respectively. ω and c are, respectively, the angular frequency and the speed of light in vacuum. The electromagnetic boundary conditions yield the relation $\frac{\varepsilon_1}{\kappa_1}+\frac{\varepsilon_2}{\kappa_2}+i\frac{\sigma}{\omega\epsilon_0}=0$ (ϵ_0 is the vacuum electric permittivity)[28,29] that, in the non-retarded regime ($q\gg\frac{\sqrt{\varepsilon_{1,2}}\omega}{c}$), leads to the SPP frequency-momentum dispersion relation $q=i\frac{2\omega\varepsilon\epsilon_0}{\sigma}$ where $\varepsilon=\frac{1}{2}\left(\varepsilon_1+\varepsilon_2\right)$ is the average dielectric function.

The strong confinement of polariton modes is attested by: (i) the ratio $\frac{\lambda_0}{\lambda_p}$ and (ii) the estimated penetration depth $\zeta_{1,2}=\left[\kappa_{1,2}\right]^{-1}$ along the z direction. In conductive 2D materials, the values of λ_p and $\zeta_{1,2}$ are much smaller than the excitation wavelength. Furthermore, the SPPs properties can be actively controlled by adjusting σ in field-effect architectures and/or by conveniently choosing the surrounding media (i.e., $\varepsilon_{1,2}$). Hence, one can postulate that the manipulation of subdiffractional SPPs means controlling light at the nanoscale. Such ability was, primarily, shown for graphene systems through regulation of its Fermi level.[30–35] These experiments were carried out with s-SNOM. Using different strategies to achieve tunability, characteristic values of λ_p in graphene, in the mid-IR, were found to range between 50 to 450 nm.[3] Recently, it was demonstrated that, in a s-SNOM experiment, the SPP propagation length in encapsulated graphene exceeds 10 µm, with the damping of the SPP wave being dependent on the temperature.[32]

Mid-IR volume confined hyperbolic phonon-polaritons (HP^2) have been intensely studied in hBN vdW crystals.[36],[1,3,15,37] Generally, HP^{2}s are supported by uniaxial crystals wherein the real parts of the in-plane $\varepsilon_\perp$ and out-of-plane $\varepsilon_{\parallel}$ projections[b] of the dielectric tensor $\acute{\varepsilon}=(\varepsilon_{\perp},\varepsilon_{\perp},\varepsilon_{\parallel})$ have different signs, meaning $\Re(\varepsilon_{\perp}).\Re(\varepsilon_{\parallel})<0$. This condition leads to hyperboloidal isofrequency surfaces (HS) in their dispersion relation[38] and, consequently, hyperbolic crystals are well known as media that are able to sustain HP^2 waves with large q. HS of type I occur for $\Re(\varepsilon_{\parallel})<0$ and $\Re(\varepsilon_{\perp})>0$, while those of type II for $\Re(\varepsilon_{\parallel})>0$ and $\Re(\varepsilon_{\perp})<0$. For hBN, a type I HS, or type I band, appears via the coupling of mid-IR photons with wavelengths ranging from 13.33 µm (750 cm^{-1}) to 12.2 µm (820 cm^{-1}), to out-of-plane polarized phonons. On the other hand, a type II band forms from the hybridization between mid-IR photons in the range 7.33 µm (1365 cm^{-1}) – 6.21 µm (1610 cm^{-1}) and in-plane polarized phonons. Accordingly, type I and type II HP^2 exist in the above-mentioned spectral ranges. HP^2 waves have been observed in hBN based systems of s-SNOM[26,39–44] and photo-induced force microscopy (PiFM).[45] They are typically launched or emitted by edges[46] and features[47] of the hBN crystal or by metallic antennas.[48] Being volume confined modes, the HP^2 λ_p is dependent on the crystal thickness[15] and also on the dielectric function of the substrate,[18,47] with $\frac{\lambda_0}{\lambda_p}$ ultimately approaching 50.[3] The short λ_p, however, results in an ultra-slow group velocity[49] of those HP^2 waves. Additionally, as will be shown in the following sections, in graphene-hBN heterostructures the coupling of HP^2 and SPP modes constitute a third type of polariton: hyperbolic plasmon-phonon polaritons (HP^3)[18,50,51]: a hybrid quasi-particle, that can be externally tuned in amplitude and wavelength by electric gating.

Although in recent years the polaritonic research has been focused on thin vdW materials, polaritons are also observable in bulk materials, as surface modes in thicker samples, or in samples with one- or zero-

---

[b] The symbols ⊥ and ‖ are defined as the parallel and perpendicular directions with respect to the crystalline optical axis c (Figure 1b).

dimensional geometry. For example, s-SNOM investigations of SiC bulk samples revealed phonon-polariton modes with theoretically predicted narrow resonances,[52]in the Reststrahlen region between 790 cm^{-1} to 950 cm^{-1}.[52],[53] Similarly, sharp resonances[53,54] from crystalline SiO_2[54,55] were observed in the 1074 cm^{-1} to 1263 cm^{-1} range. The sharpness, width and frequency of these near-field responses depend on the sample thickness.[55]

1.2. Synchrotron Infrared Nanospectroscopy (SINS)

Along with advances in the preparation of new and novel materials, characterization techniques have developed at an accelerated pace and have significantly expanded their analysis capabilities. In the context of 2D materials, many open scientific questions involve the electronic, optical and chemical properties in nanometric regions, such as defects, interfaces and edges. Scanning Tunneling Microscopy (STM), Transmission and Scanning Electron Microscopy (TEM, SEM) and AFM are established techniques for atomic and nanometric analysis of material surfaces covering properties such as morphology and local work function. However, they are not suitable for studies that require chemical or optical analysis of heterogeneous nano-domains. On the other hand, optical characterization techniques, such as fluorescence optical microscopy, Raman microscopy and infrared spectro-microscopy, have long been established for the determination of optical properties and the chemical identity of materials in a non-invasive manner with low operation cost and simple requirements for sample preparation. However, such techniques are based on far-field optics with spatial resolution defined by the diffraction limit of light. Hence, in the best optical and spatial resolution conditions, these classical far-field techniques are limited to resolving regions or structures not smaller than $\sim\lambda/2$. For analyses that require long-wavelength radiation, such as Fourier transform infrared (FTIR) in the mid-IR and far-IR ranges, the spatial resolution is typically a few microns or larger and, thus, unviable for analysis of isolated nanostructures or submicron 2D systems.

In this scenario, near-field optics techniques, such as s-SNOM, have significantly boosted the findings in the areas of nano-optics and nano-chemistry of 2D materials.[14,15,63–67,33,56–62] In the field of broadband vibrational nanospectroscopy, s-SNOM is an established nanoprobe tested with various light sources, such as classic blackbody sources,[68] broadband lasers[69] and, more recently, synchrotron IR sources.[35],[24,70,71] In this last configuration the technique has achieved unprecedented potential given the high spectral irradiance of the synchrotron sources (up to 1000 times greater than the brightness of a thermal source[72]) with ultrawide emission spectrum covering the entire IR range (near to far-IR).

The SINS technique exploits the principle of converting free propagating waves, generated by a synchrotron source, into evanescent fields at a sharp tip via the antenna effect. A metallic AFM tip is illuminated by the light beam that polarizes the free charges of the antenna and thus creates extremely confined electric fields at the tip apex surface (Figure 2a). In this configuration, the volume of the confined fields at the tip is defined by the tip form factor and no longer depends on the wavelength of the incident radiation (breaking of the diffraction limit), enabling a light probe with spatial resolution comparable to the radius of commercial AFM tips, typically less than 30 nm. The sample is then brought into semi-contact with the tip by a 3D piezoelectric stage as in the classic AFM "tapping mode" experiments. Through interaction with highly dense electric fields at the tip apex, the surface of the material is locally polarized and thus produces a scattered wave which carries nanometric dielectric information of the sample (Figure 2b).

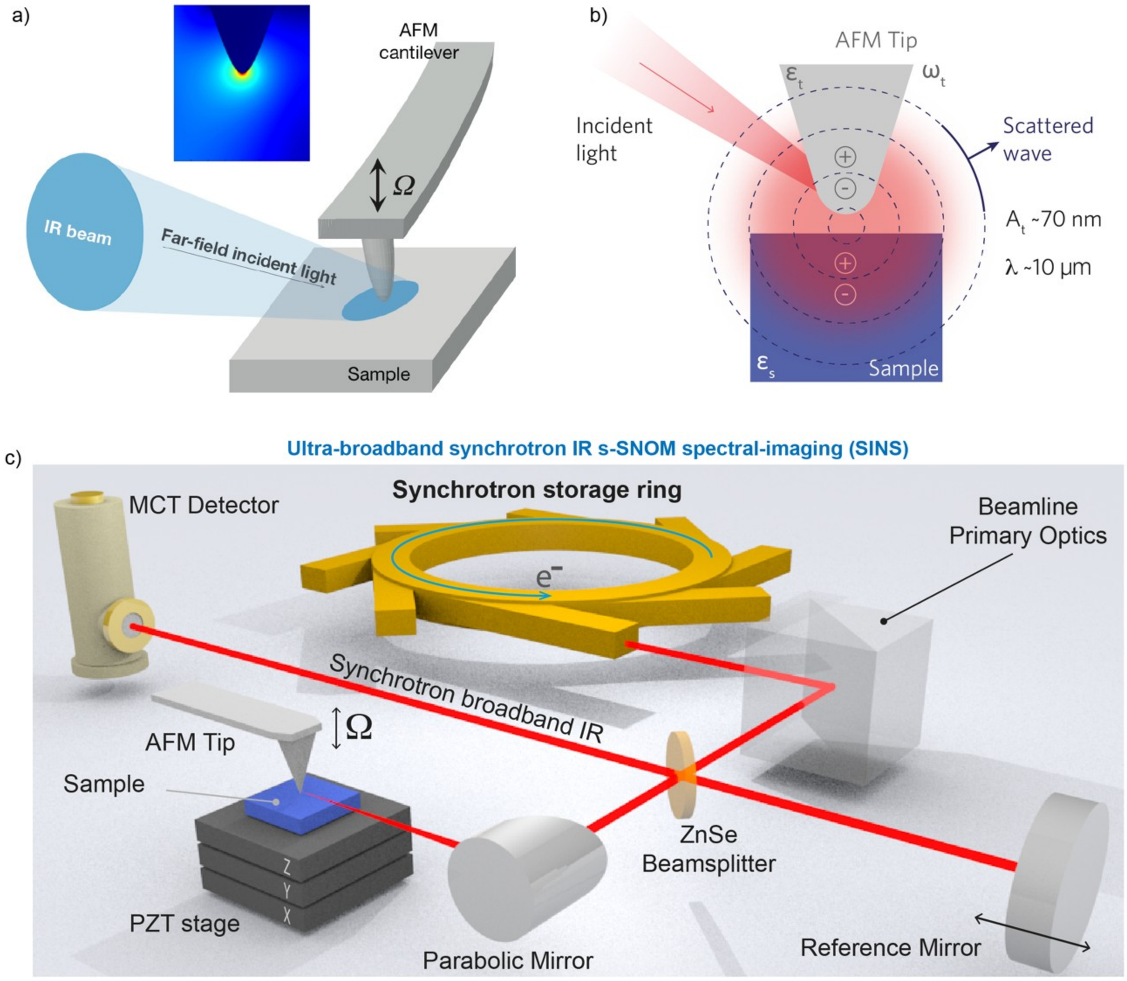

Figure 2 - Principle of the SINS technique and its interferometric scheme for broadband spectroscopy. (a) Illustration of the principle of confinement of free-space electromagnetic waves by a nano-antenna (metallic AFM tip) in s-SNOM. Inset: simulation of the confined electric fields near the nano-antenna apex with dimensions comparable to the radius of the tip.[73] (b) Scheme of the interaction of the evanescent electric fields at the tip (near-field) with the surface of the sample. (c) SINS scheme, including excitation of the s-SNOM by a synchrotron source and an FTIR-like Michelson interferometer. Figure (c) adapted from R. O. Freitas *et al.*,[25] Copyright 2018, OSA.

For spectroscopic detection of the scattered fields from the tip-sample interaction, the AFM stage and the s-SNOM optics are mounted in an interferometer, as shown in Figure 2c. The suppression of the far-field background produced by the illumination is performed by lock-in demodulated detection at high harmonics of the natural frequency of the AFM tip.[22] In this asymmetric interferometric arrangement, SINS is sensitive to the amplitude and phase of the scattered wave, which is proportional to the local complex dielectric response of the material analyzed.[74] The interferometric arrangement is also used for demultiplexing the various wavelengths of the broadband incident photons via Fourier processing, similar to classical FTIR experiments.[75] As an AFM-based experiment, SINS simultaneously obtains nanometric information of topography and broadband optical response from the surface of the material. SINS can acquire such optical response from different measurement modalities as point-spectrum, spectral linescan and hyperspectral image. In the following, it is described how each of those measurements are employed to retrieve information on polaritons.

1.3. Extracting fundamental polariton properties from SINS data processing

As commented above, the SINS sharp metallic tip, illuminated by an incident broadband IR beam, becomes a nanosized optical source with large momentum components that are able to excite radial polariton waves (Figure 3a). In this case the tip acts as a reception antenna, transducing the incoming far-field into near-field that causes a local effective polarizability of the interacting media (sample). Simultaneously, the same tip captures the resulting optical near-field and converts it back into far-field radiation, which is sent to the detection system, thus working as an emitting antenna. Due to the antenna property of the tip, SINS measurements (Figure 3b-l) enable full characterization of the polariton dynamics in the sample, including structure-related features, such as spatial modulation of the polaritonic wave provided by interference between tip- and edge-launched waves (Figure 3c), as well as material-related features, which are modulated by the material's dielectric function and are provided by the non-propagating optical fields (NOF) response. The NOF is evidenced when the tip probes an area far from crystal edges or any other eventual polariton launcher, as displayed in Figure 3b. In such a circumstance, although the tip launches polaritons, they are not directly detected/imaged, as they fade out before reflecting back to the tip-probe. Typically, the NOF response, which can be acquired from a point-spectrum in the middle of the crystal as suggested in Figure 3d, presents only information about the dielectric resonances of the Reststrahlen bands (Figure 3e). On the other hand, the tip- and edge- launched polariton waves can be visualized from a spectral linescan across the crystal edge (Figure 3f). This measurement comprises of a set of equally spaced point-spectra collected while the tip scans a path. Accordingly, a spatio-spectral map (Figure 3g) is generated, featuring intensity modulations from the resulting interference of the polariton waves associated to all ω's in the Reststrahlen band. The polariton wave amplitude profile (Figure 3h), for a certain ω (ω = constant), is extracted from the spatio-spectral map by plotting the amplitude versus position (green dashed line in Figure 3g). Using different analysis methods (see next section), the complex polariton momentum $Q=q+i\kappa$, where κ is the damping, is determined and compared with theoretical frequency-momentum dispersion relations (Figure 3i). Furthermore, analogue properties of the polariton field can be recovered from SINS hyperspectral images (Figure 3k), which are constructed from an array of full single-point spectra, that provides 2D polariton maps carrying equivalent information as those obtainable from the spectral linescan as suggested by the interconnection between Figure 3l and 3h.

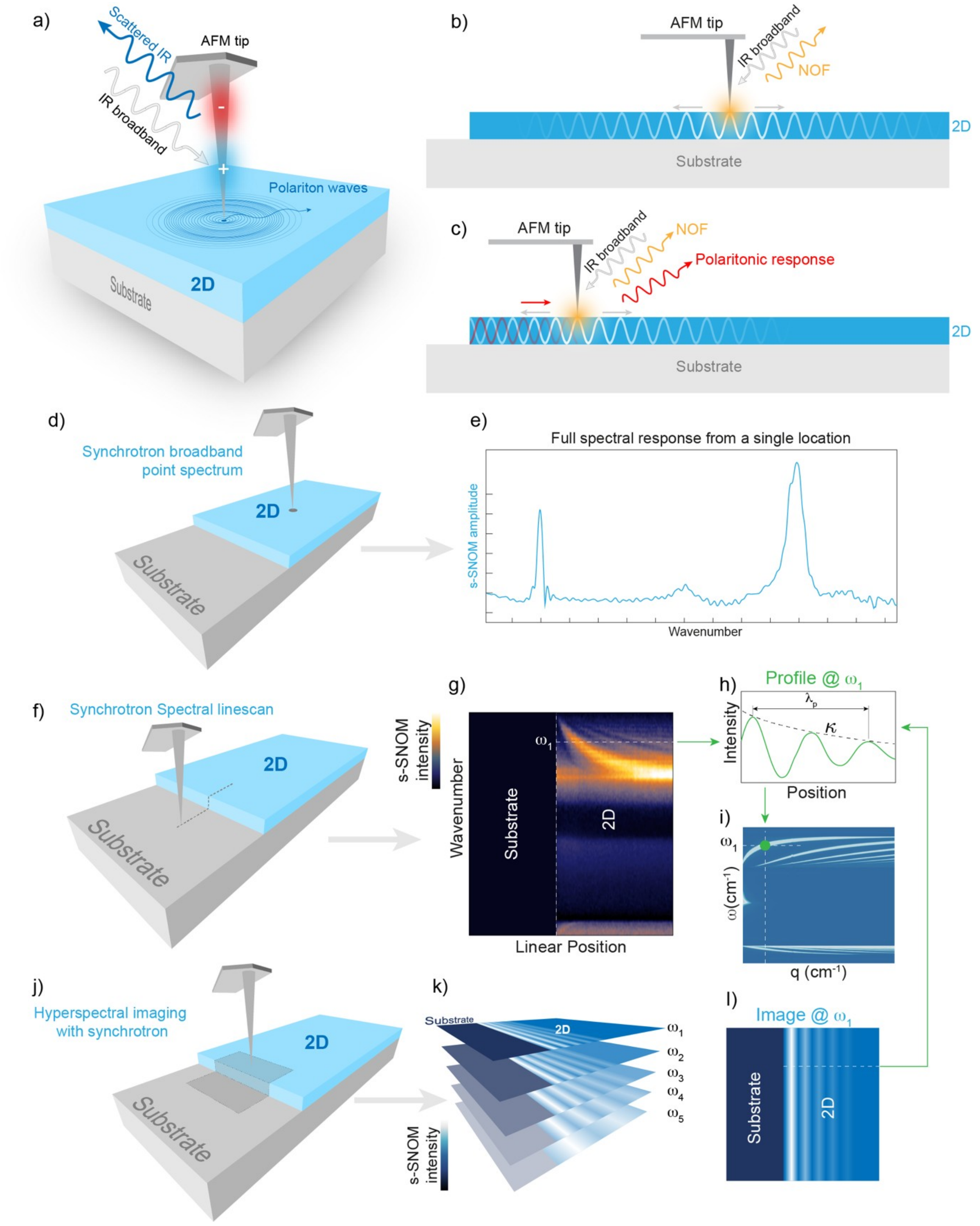

Figure 3 – SINS measurements of vdW polaritonic crystals. a) Illustration of the incident IR light producing charge separation and consequent polarization to the AFM tip. Accordingly, the tip confines optical field with the high momenta required to launch subdiffractional polaritons. b) NOF measured by the tip in the middle of the crystal. c) tip- and edge-launched polaritons and the NOF composing the total near-field probed by the tip close to the crystal edge. d) Scheme of a point spectrum measurement in a crystal location far from edges. e) Typical NOF without contributions from the propagating polaritons. f) Scheme of a typical spectral linescan across the edge of a 2D crystal with its corresponding spatio-spectral map (g) featuring intensity modulations from the

interference of polaritonic waves. h) Polariton wave profile for a frequency ω_1 obtained from (g). i) Example of theoretical frequency-momentum dispersion relation typicaly applied to interpret SINS data. j) Scheme of a hyperspectral image measurement with the tip scanning an area (shadowed region) across the crystal edge and substrate. k) Images of polariton standing waves, for selected ω's, generated by post-processing the hyperspectral data. l) Polaritons image for ω_1.

2. SINS and the polaritons in hBN-based structures

2.1. Polaritons in hBN and graphene-hBN heterostructures

One of the great advantages of SINS is the full coverage of the IR fingerprint in a “single-shot” fashioned nanospectroscopy experiment. This feature is especially attractive for the study of systems with multiple vibrational signatures inside a wide spectral range. This is the case for hBN, which possesses Reststrahlen bands at very distinct frequencies (~800 cm^{-1} and ~1500 cm^{-1}). Therefore, SINS enables simultaneous measuring of the two hBN bands with rigorously the same conditions, allowing a precise comparison between the material’s nano-optical response in those two different frequency ranges. In this context, SINS linescans and hyperspectral maps of hBN crystals, can provide a direct view of polaritons waves in a multifrequency domain. Figure 4a and Figure 4b show spatio-spectral maps of SINS amplitude and phase, respectively, obtained by a spectral linescan across the edge of an hBN crystal lying on SiO_2.[76] Both maps reveal the intensity contrasting modulations of the type I and type II polaritons. Figure 4c and Figure 4d present amplitude (blue curves) and phase (red curves) profiles at fixed frequencies in the type II band, extracted from Figure 4a and Figure 4b, respectively. In this case, the resulting polaritonic field can be understood as the interference of tip-, edge-launched polaritons and the NOF component. The tip launches polaritons that propagate to the crystal edge, wherein they reflect and propagate back to the tip, while edge-launched waves travel directly to the tip. The tip, then, probes the optical field resulting from the interference of all those fields as depicted in the scheme of Figure 3c. The determination of the polariton momentum is, usually, done by fits to theoretical modellings or by the Fourier Transform of the wave profiles extracted from spatio-spectral linescans and/or hyperspectral images, as discussed above. The fit models, in general, consider the resulting optical field created by the all effective polariton launchers of the system: tip, edge and antenna-like structures (see, for example,[42]). Different complex-valued fields, based on damped sine or geometrically decaying functions, have been proposed to simulate or fit polariton waves. As in s-SNOM and SINS, the tip is a probe, therefore the fields of each launcher are defined as a function of the relative distance between the tip and other sources.

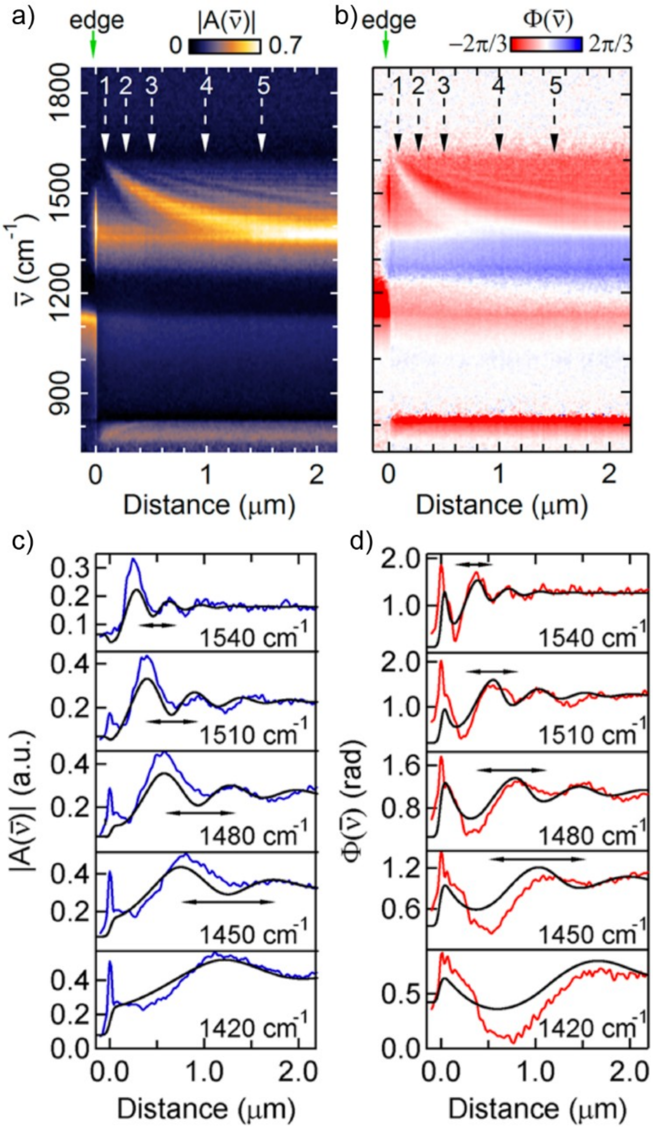

Figure 4 - a) Amplitude and b) phase of a spatio-spectral linescan taken across the edge of an hBN crystal on SiO_2. c) Experimental amplitude (blue curves) and (d) experimental phase (red curves) profiles of type II HP2 waves extracted from the measurements in a) and b), respectively. The black curves are theoretical fitting. In this figure, the authors adopted the wavenumber $\acute{\nu}$, with $\acute{\nu}=\frac{1}{\lambda_0}$, to refer to the IR excitation. This figure is reproduced from reference [76]. Copyright 2015: The American Chemical Society.

Hybrid polaritons with multiple sources have been observed in a graphene-hBN heterostructure lying on an Au-air heterointerface (Figure 5).[18] Such hybrid modes consist of the coupling between graphene SPPs and hBN HP^2s creating hyperbolic plasmon phonon-polaritons (HP^3) modes. As illustrated by the device cross section scheme in Figure 5a, upon far-field IR illumination, the tip and the Au edges, underneath the graphene-hBN structure, are turned into polariton sources. Tip-launched waves propagate toward the air-Au transitions on both sides, where they partially reflect and travel back to the tip. The reflection occurs because the graphene-hBN dielectric environment changes substantially from air to Au, leading to different polaritonic mode structures on the air and Au regions. On the other hand, edge-launched waves of both sides propagate directly to the tip. Hybrid polariton fields, resulting from the interference between those fields, are shown in SINS hyperspectral images (Figure 5b) over the graphene-hBN/(air-Au) sample region.

Considering the reference frame of Figure 5a, the field components generated by the tip, one propagating in the $+x$ and the other in the $-x$ directions, are given by the first and second terms of equation 1, respectively. In this expression, A is the amplitude, α_0 and $\alpha_1$are constant phases and q_1 is the complex momentum of the zeroth-order mode of the HP^3 wave. The third term in equation 1 is the NOF. The components launched by the edges are given by equation 2, with β_0 and $\beta_1$being constant phases and B_0 and B_1 amplitudes of the waves emitted from the left and right Au edges, respectively. Accordingly, the resulting optical field is $\xi_{Opt}=\xi_{tip}+\xi_{Au\,edges}$. Figure 5c shows ξ_{Opt} fits to the polariton profiles, on the air and Au sides, obtained from the hyperspectral images in Figure 5b. One finds that q on air is substantially lower than on Au, thus, corroborating the observation of reflection due to dielectric-metal substrate transition.

$$\xi_{Tip} = \mathrm{A}\left(\frac{e^{-i\alpha_0} e^{i(q_1+i\kappa_1)2x}}{\sqrt{2x}} + \frac{e^{-i\alpha_1} e^{i(-q_1+i\kappa_1)2(x_{edge}-x)}}{\sqrt{2(x_{edge}-x)}} \right) + Ce^{-i\eta} \qquad \text{Eq. 1}$$

$$\xi_{Au\ edges} = B_0 \frac{e^{-i\beta_0} e^{i(q_1+i\kappa)x}}{x} + B_1 \frac{e^{-i\beta_1} e^{i(-q_1+i\kappa)(x_{edge}-x)}}{(x_{edge}-x)} \qquad \text{Eq. 2}$$

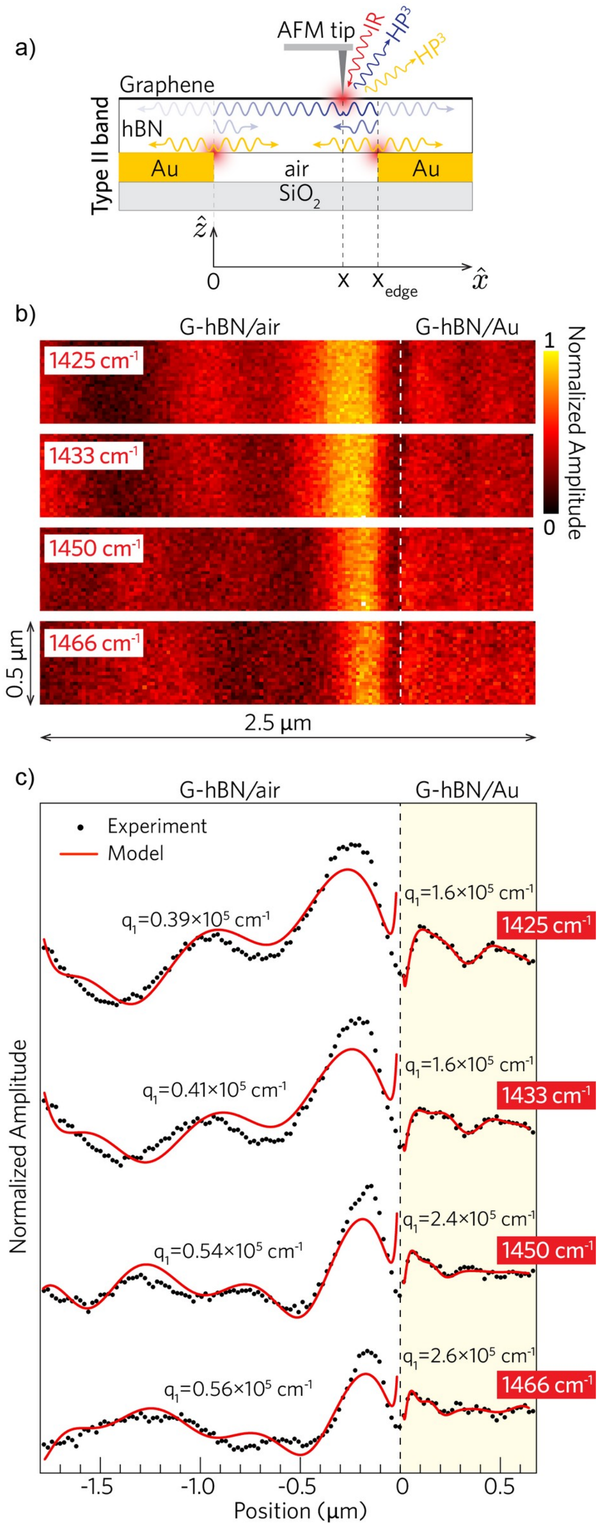

Figure 5 a) Scheme of the graphene-hBN device and reference frame adopted to explain the polariton waves originated from multiple sources in the sample. b) Narrowband spatial maps of the SINS amplitude reconstructed from hyperspectral imaging of the type II hybrid polaritons of the graphene-hBN heterostructure lying on the air-Au interfaces. c) Average amplitude profiles (dots) of the amplitude maps in (b) and curve fits (red curves) considering multiple polariton sources. Reproduced from [18]. Copyright 2019: The American Chemical Society.

2.2 Phonon Polariton-assisted Infrared Nanoimaging of Local Strain in hBN

The intentional application of mechanical deformations in condensed matter physics provides an extra degree of freedom to modify the intrinsic properties of a material.[77,78] For instance, in conventional semiconductor manufacturing strain engineering is employed to enhance opto-electronic devices performances. In this case, systematic straining is applied to modify the electronic band structure, thus affecting valley splitting[79,80] and effective masses.[34,81] In 2D materials, large strain can be achieved without breaking the material. Elastic deformations up to 25% have been demonstrated in monolayer graphene.[82] Moreover, strain effects are more pronounced and may lead to novel electronic states in thin 2D materials, such as the generation of strong gauge fields that effectively act as strong magnetic fields,[83–85] or local confinement potentials through the modification of the electronic band structure.[86,87]

The large bandgap in 2D hBN makes this material system very promising for atomically thin flexible devices. At the same time it shows a high mechanical strength so that it has been proposed as a reinforcing material in composites.[88] Furthermore, due to its insulating properties it enjoys frequent application in 2D heterostructures,[89] where lattice mismatch may lead to undesired or desired strain. It is therefore of great importance to noninvasively characterize the mechanical strain fields in hBN. The level of strain in the crystal structure may be quantified by phonon shifts using Raman spectroscopy,[87] which requires knowledge about the shift rate of the corresponding Raman mode. Recently, the strain-induced phonon shift of mechanically exfoliated hBN of various thickness has been determined.[90] Complementary to Raman spectroscopy also infrared (IR) active phonon modes may be used for quantifying the strain. At high spatial resolution such a strain map has been obtained using phonon-polariton modes on the surface of 3D bulk semiconductors[91] using IR SNOM. Because strain is a tensor of rank two, a quantitative deduction from the phonon–polariton excitations is challenging. Yet, in 2D hBN crystals a quantitative analysis of a local strain field has recently been demonstrated Lyu *et al.*[92], which is summarized in the following.

A typical local strain profile arises from the formation of wrinkles after an annealing process. Here hBN flakes, mechanically exfoliated onto a SiO_2/Si substrate from the bulk hBN crystal, experience a mismatch in the thermal expansion coefficient between the hBN (negative) and the Si substrate (positive). In the region near the end of the wrinkle an in-plane local compressive strain arises. When imaging the hBN crystal near in-plane TO phonon frequency (type II band), ω_{TO} = 1372 cm^{-1}, the strain profile can be visualized owing to the strain dependent phonon shifts, shown in Figure 6a. In the absence of any topographical features, dark spots indicate a detuning of the phonon mode away from resonance accompanied by a change in the local dielectric function. Such dark spots appear near the wrinkle ends in Figure 6a marked by arrows, in this case resulting from the compressive strain and a corresponding blue-shift of the phonon resonance.

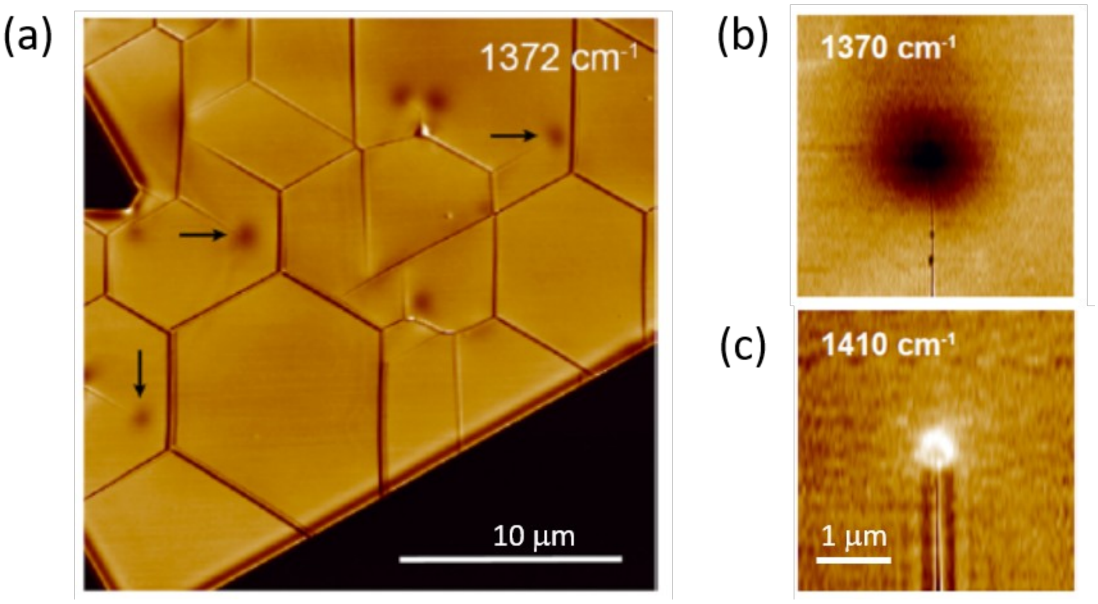

Figure 6 - (a) Narrowband near-field IR image of the annealed hBN flake (~6 nm thick) with wrinkles on a SiO_2/Si substrate, taken at a frequency of 1372 cm^{-1}. The arrows denote the dark spots near the wrinkle ends. (b) and (c) are zoomed IR images at the indicated frequencies. Adapted from Lyu *et al.* [93], Copyright 2019 American Chemical Society.

In addition to the local dielectric function, the propagating phonon polaritons result in another contrast mechanism at certain frequency, namely where phonon polariton reflection and interference occur. Figure 6b shows again a zoomed s-SNOM narrowband image at a slightly lower frequency of 1370 cm^{-1}. In contrast, at frequencies higher than 1372 cm^{-1}, the near-field excitation launches propagating nonlocal phonon polaritons. Upon partial reflection at the strained region due to a gradient in the dielectric function, the scattered nearfield signal at the tip position will be modified. Figure 6c shows this case, where the originally dark spot has become bright and features appear along the strained wrinkle. These features have been interpreted in terms of a combination of the change in the local dielectric function and propagating nonlocal phonon polaritons.

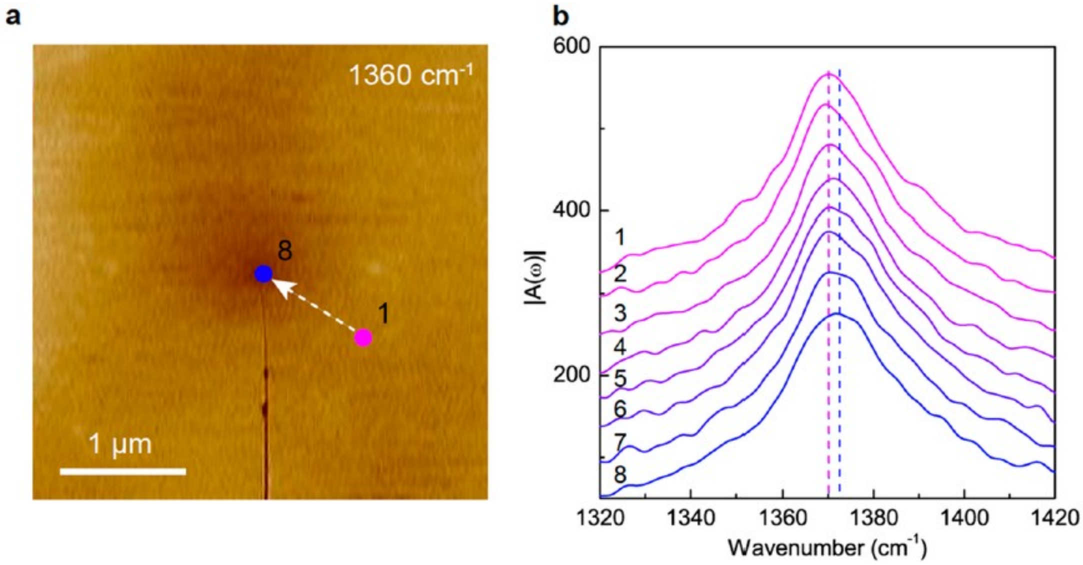

Figure 7 - (a) Narrowband near-field IR image of a 5 nm thick hBN sample, excited at 1360 cm^{-1}. (b) SINS point-spectra along the line shown in (a). Adapted from Lyu *et al.* [93], Copyright 2019 American Chemical Society.

For a quantitative analysis, the strain-induced shifts of phonon frequencies are directly measured with the assistance of SINS. Figure 7a shows the path in the narrowband near-field IR image along which a series of spectra has been recorded. A frequency shift of 2 cm^{-1} is observed as the center of the strained region (Figure 7b). A quantitative relation of the measured hBN TO phonon frequency under strain was calculated using first-principles density functional theory (DFT) within the local-density approximation (LDA), which allowed extracting the strain from the experimental SINS spectra. With a minimal detectable frequency shift of 0.5 cm^{-1} in this setup, the authors conclude that a minimum strain of 0.01% can be detected using this method.

3. Mid-IR localized plasmons in individual metal-oxide nanocrystals

Doped metal oxides, such as indium-doped tin oxide (ITO), aluminum-doped zinc oxide (AZO) and gallium-doped zinc oxide have received increased attention from the photonics community, as they present near-zero dielectric functions (epsilon near zero behavior) at near infrared wavelengths, bringing about a number of applications as substrates for plasmonic metallic nanoantennas[94] and materials for extreme nonlinear optics.[95] Presenting a negative dielectric function beyond the epsilon near zero point (i.e., longer wavelengths), they support surface plasmons in the mid-infrared. Indeed, a number of reports have focused on the synthesis of doped metal oxide nanoparticles, the observation of mid-infrared localized surface plasmon resonances, and their use for enhancing light interaction with molecules.[96–99]

Figures 8a and 8b respectively show AZO and ITO nanoparticles with lateral sizes of a few tens of nanometers.[100] They clearly show size and shape heterogeneities, which may in principle affect their plasmonic properties. Figure 8e (dashed) show the corresponding extinction spectra as measured with a far-field FTIR spectrometer, which inevitably probes a large nanoparticle ensemble. The spectra, centered at about 2000 cm^{-1} and 2500 cm^{-1}, for AZO and ITO respectively, show a ~1500 cm^{-1} full width at half maximum (FWHM), which may be a consequence of homogeneous and inhomogeneous broadening. While inhomogeneous broadening may have a number of origins related to particle-to-particle fluctuations, homogeneous broadening is associated to plasmon damping, which decreases the field enhancement offered by the nanoparticles.

Homogeneous and inhomogeneous broadening may be distinguished by measuring the extinction spectrum of individual nanoparticles. In metallic nanoparticles, presenting plasmonic resonances in the visible spectral range, this can be accomplished via a number of far-field methods,[101–103] by focusing the excitation light and exploiting the large plasmonic scattering cross section. However, the ten-fold increase in wavelength in the mid-infrared relative to the visible results in three orders of magnitude increase in the diffraction limited modal volume, decreasing the light-particle interaction signal beyond detectability.

To probe individual AZO and ITO nanoparticles, Johns *et al.*[100] used SINS. Synthesized nanoparticles were spin coated on a gold substrate and the substrate proximity with the conductive AFM tip (<25 nm apex) created a near-field hot spot for the incident synchrotron radiation, which lead to the increased overlap between radiation and nanoparticle. The extinction spectrum of individual particles was, then, clearly identified (Figures 8c and 8d). These nanoparticles are, so far, one of the smallest objects from which SINS spectra were obtained.[100] Spectra taken from the same nanoparticle were reproducible and presented a blue shift relative to the far field, which is an expected feature from tip-sample interaction. Notably, the near-field spectra presented FWHM that was less than half that of the ensemble (far field), and as low as 600 cm^{-1} (Figure 8e). This feature indicates that the ensemble linewidths are dominated by inhomogeneous broadening. The narrower single particle linewidths highlight the low plasmon damping in doped metal oxide, which is lower than in metal nanoparticles.

Correlation between individual SINS spectra (Figure 8c) and AFM topography (Figure 8d) indicated no clear relation between spectral variations and particle height. On the other hand, a statistically significant correlation between plasmon resonance energy and peak asymmetry was found, indicating that the inhomogeneous broadening may be a consequence of particle-to-particle variations in dopant incorporation beyond what is expected from a Poisson distribution. Advances in the synthesis methods are, thus required for improving homogeneity.

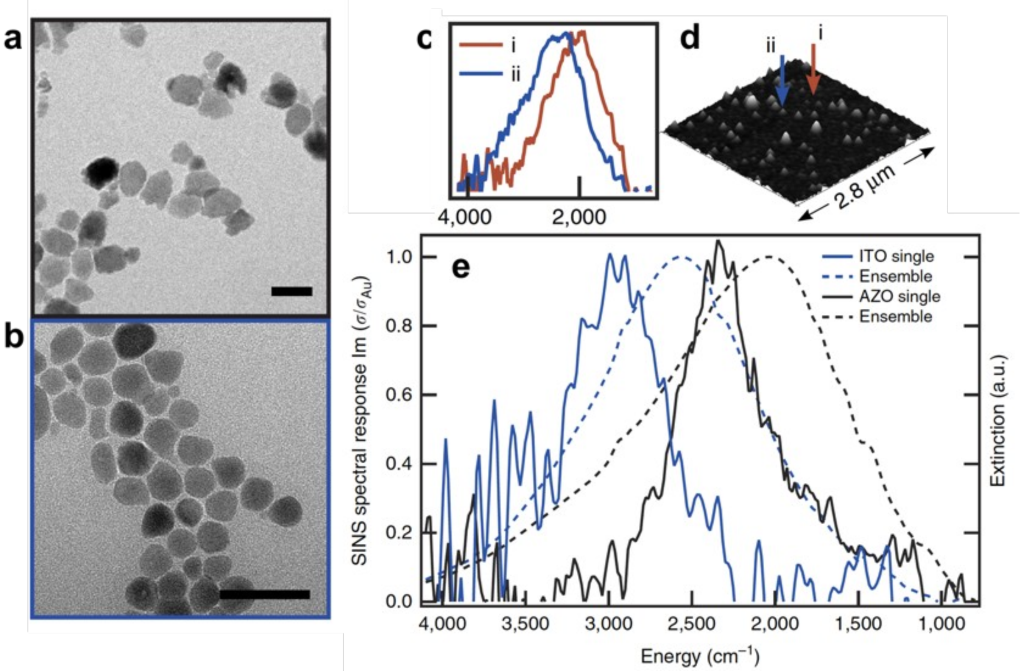

Figure 8 - Transmission electron microscopy images of AZO (a) and ITO (b) nanoparticles. SINS spectra of individual nanoparticles (c) and correlation with the corresponding AFM topographic data (d) for AZO nanoparticles. (e) SINS (solid) and far-field (dashed) spectra of AZO and ITO nanoparticles. Adapted under the terms of the CC BY 4.0 license.[100] Copyright 2016, Springer Nature.

4. Nanoscale plasmonic phenomena in CVD-grown MoS_2 single layers

Transition metal dichalcogenides (TMD) consist of hexagonally structured layers of transition metal atoms, typically Mo or W, embedded between two layers of chalcogenides (typically S, Se, or Te).[104] TMD bulk crystals are formed of monolayers bound to one another by van-der-Waals attraction, allowing thinning down to one atomic layer, thus producing new physical properties compared to the bulk. Since the discovery of a direct bandgap for various monolayer TMDs,[105] much research has been devoted to potential applications in electronics [105] and valley physics [106]. As with graphene and hBN, discussed above, TMDs can be combined with these and other 2D materials in van der Waals heterostructures as building blocks for many different devices with large impact on nanotechnology.[4]

Of particular interest have been their plasmonic properties [107–110], partially because of their potential in plasmonic circuitry.[111,112] Specific emphasis was put on the plasmonic properties of single layer MoS_2 (1L-MoS_2),[110] which has shown that the damping is related to the collective charge oscillation entering the intraband electron hole continuum. While photoluminescence measurements is possible by the use of photons with energies exceeding the bandgap,[113] the direct excitation of the intraband plasmons requires IR radiation. However, the wavevector of plasmons in extended 1L-MoS_2 is much larger than the wavevector of freely propagating IR photons of the same energy. This mismatch can be overcome by confining IR radiation to a nanosized scattering object resulting in increased coupling into the in-plane momentum component[31,55,59,114] as in the s-SNOM technique.

In this way, the plasmon-phonon coupling of 1L- and 2L-MoS_2 has been studied[115] employing SINS. The MoS_2 layers have been grown by chemical vapor deposition (CVD) onto a 300 nm thin SiO_2 – layer on a Si substrate. In Figure 9a the SINS spectra from 1L-MoS_2, 2L-MoS_2 and the plain SiO_2 are shown. All spectra are dominated by an intense feature at ω_{SP1} = 1132 cm^{-1}. This is due to the surface phonon-polariton of the SiO_2 substrate. Additionally, a less intense feature at 794 cm^{-1} is observed due to a second surface phonon, occurring close to the transverse optical phonon frequency of SiO_2 (ω_{SP2} = 797 cm^{-1}).

A slight enhancement of the intensity of ω_{SP1} on 1L – MoS_2 and 2L – MoS_2 is revealed. The feature at ω_{SP2} is only enhanced for 2L – MoS_2 and slightly redshifted. The main features of the measurements can be reproduced within the point-dipole approximation modelling the AFM tip, as shown in Figure 9b. The reflection coefficient of the *p*-polarized field, r_p, describing the electrodynamics at the MoS_2-SiO_2 interface is given by

$$r_p(q,\omega) = \frac{\varepsilon_1 k_0 - \varepsilon_0 k_1 + \dfrac{4\pi k_0 k_1 \sigma}{\omega}}{\varepsilon_1 k_0 + \varepsilon_0 k_1 + \dfrac{4\pi k_0 k_1 \sigma}{\omega}} \qquad \text{Eq. 3}$$

where ε_0 und ε_1 are the dielectric functions of vacuum and SiO_2, respectively. σ denotes the in-plane conductivity of MoS_2. The out-of-plane components of the momenta for vacuum and SiO_2 are $k_{0,1}$ while q denotes the in-plane component. Both TO phonons have been accounted for in ε_1. Because of the different energies of the surface phonon modes of MoS_2 and SiO_2 no significant hybridization and hence no significant shift of the *s*-SNOM spectra is anticipated.

The simulated spectrum in Figure 9b confirms that only for the 2L-MoS_2 there is a small spectral shift relative to the surface phonon peak of bare SiO_2, in agreement with the measurements at 794 cm^{-1}. The observed and simulated redshift is interpreted as arising from out-of-plane SiO_2 phonon and the 2L-MoS_2 plasmon excitations. The fact that the corresponding coupling does not lead to a shift of the 1132 cm^{-1} mode in both 1L- and 2L - MoS_2 cases can be explained by the almost vertical orientation of the tip-sample that leads to a preference for coupling predominantly to vertically oscillating modes.

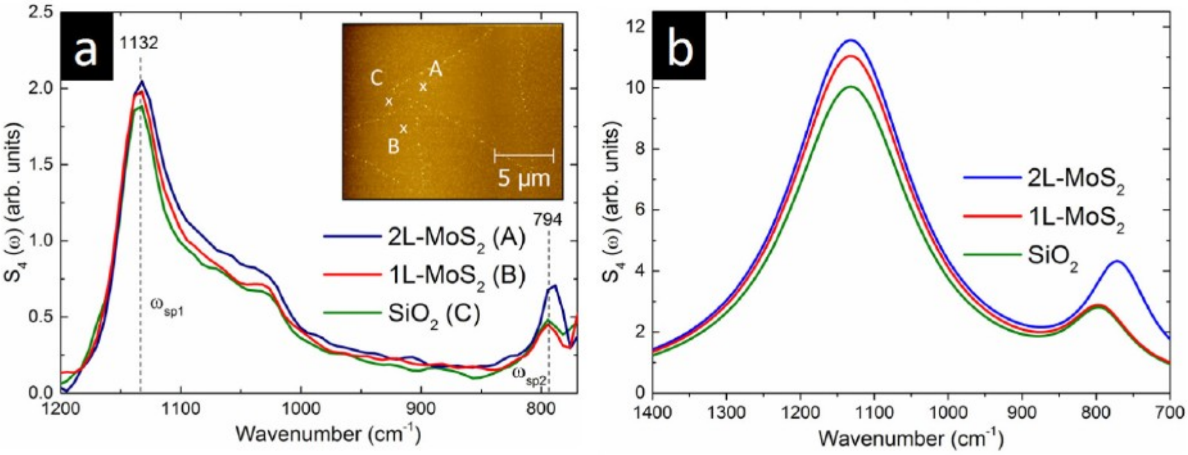

Figure 9 - (a) SINS spectra (4th harmonic) from the 3 positions on an MoS_2 flake, as shown in the inset. The layer configurations A, B and C are 2L-MoS_2, 1L-MoS_2 and SiO_2, respectively. (b) Theoretically predicted scattering signal (s-SNOM 4^{th} harmonics) of the corresponding layer configurations in (a). Adapted from Patoka *et al.* [116], Copyright 2016, OSA.

5. Hybrid polaritons in graphene-talc 2D heterostructures

Graphene plasmonics and the phonon-polariton properties of talc (Figure 10) a natural atomically flat vdW crystal, have been studied in a graphene-talc nanophotonic device using SINS.[117] As in graphene-hBN heterostructure, hybrid plasmon phonon-polaritons were identified in graphene-talc (Figure 11a) revealing appealing aspects for photonic applications.[118–120] Regarding applications in 2D electronics, talc is a compelling insulator media, with a band gap ~5.3 eV[121] (Figure 10d) as predicted from density functional theory (DFT), directly competing with the well-established insulators SiO_2 and hBN. Recently, in graphene-talc devices, spontaneous high *p*-type doping of graphene has been observed, as well as excellent charge mobility and the quantum Hall effect.[122,123]

The talc crystal investigated is a natural soft magnesium silicate mineral, with chemical formula $Mg_3Si_4O_{10}(OH)_2$, obtained from a soapstone mine in Ouro Preto, Brazil.[124–126] This vdW crystal forms, by mechanical exfoliation, flat crystals with nanometer thicknesses, as observed with AFM topography (Figure 10b). Also, SINS broadband image (Figure 10c) unveils sharp contrast among the talc layers and the SiO_2 substrate. Moreover, SINS point spectra at different thicknesses, on a gold substrate, (Figure 10e) show IR resonances assigned to SiO_4 vibration around 990 (ν_3) and 1010 (ν_2) cm^{-1}, as well as OH libration modes around 670 (ν_1) and 690 (ν_{out}) cm^{-1}. Considering the symmetry of those vibrations, ν_1 and ν_3 are in-plane modes, whist ν_2 and ν_{out} are out-of-plane vibrations. As with hBN, such resonances are dependent on the crystal thickness.

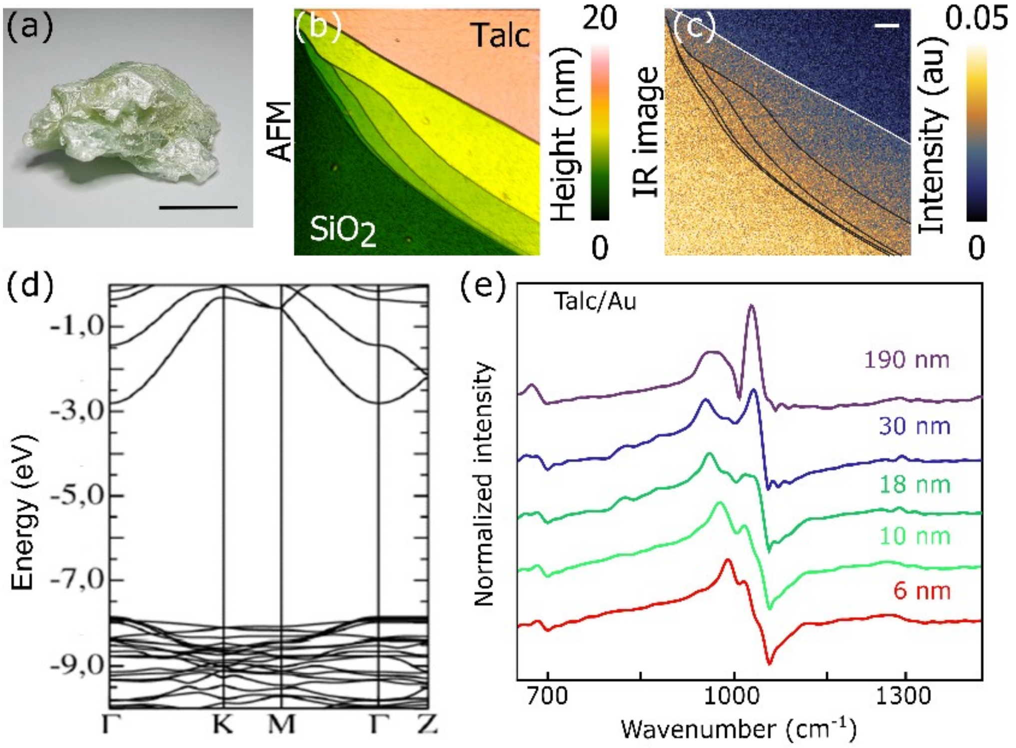

Figure 10 - (a) Photograph of a large mineral talc crystal from a soapstone mine in Ouro Preto, Brazil. Scale bar is 1cm. (b) AFM topography of layers of talc on a SiO_2 substrate. (c) IR broadband nearfield image of the same regions shown in (b); the scale bar represents 1 µm. (d) DFT calculated electronic band structure for bulk talc. Reproduced with permission from [127] under the terms of the CC BY license. Copyright 2016, IOP Publishing Ltd. (e) SINS point spectra of a talc nanocrystal as a function of the crystal thickness on a gold substrate. Copyright 2018, The American Chemical Society.

The graphene-talc heterostructure, mounted in a field effect transistor architecture (Figure 11a and Figure 11b), features an atomically flat surface, stable and free of detectable defects.[121],[117,122] In Figure 11c one notes from SINS point-spectra that the 1025 cm^{-1} out-of-plane mode is significantly increased for graphene-talc compared to pure talc. In contrast, graphene mildly affects the 960 cm^{-1} mode. As can be seen in the transfer curve in Figure 11d, the charge neutrality point of the graphene-talc/Au device is reached around the back-gate voltage (V_G) value of 32 V, highlighting a naturally induced high p-doping. A clear amplitude modulation of the 1025 cm^{-1} mode is demonstrated by varying V_G in the 0 – 25 V range (Figure 11e). Those results indicate a clear coupling between graphene plasmons and the talc phonons leading to the formation of hybrid plasmon phonon polaritons. This hybridization is confirmed by the blue-shift of the hybrid mode in the theoretical $\omega - q$

dispersion of the graphene-talc system in the high p-doping condition (n ~ 6.5 × 10^{12} cm^{-2} corresponding to V_G = 0V), as shown in the right panel of Figure 11f, in comparison with pure talc, left panel in Figure 11f.

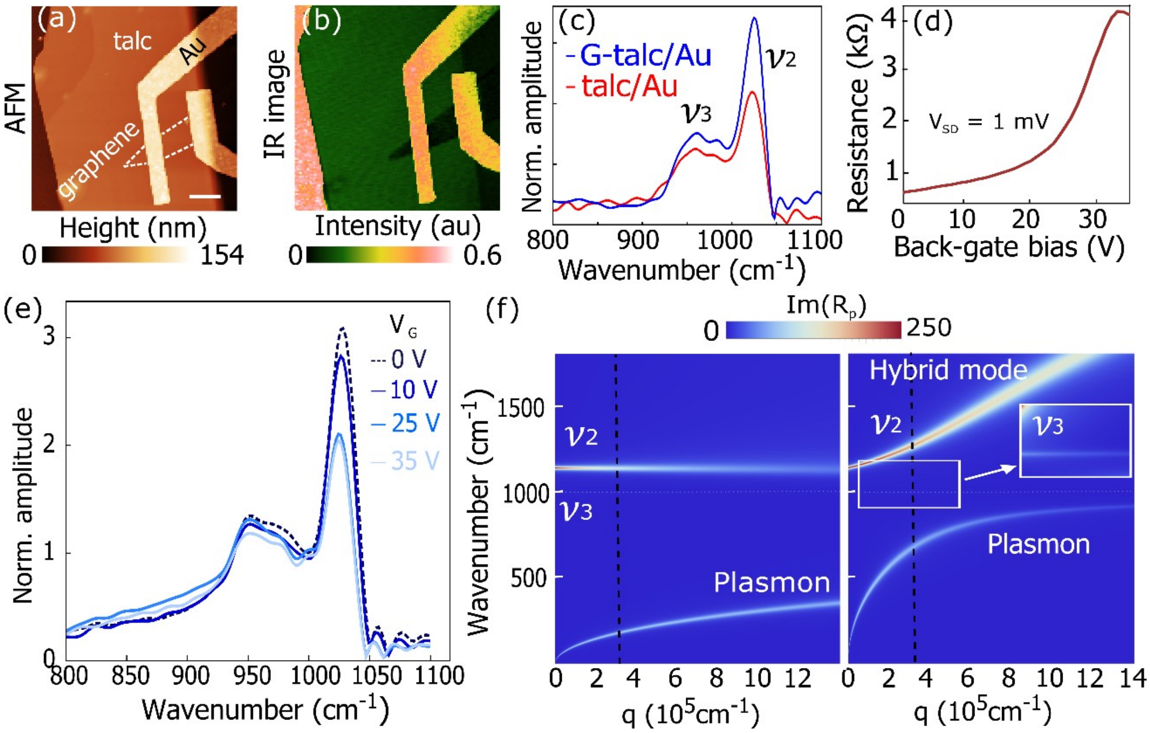

Figure 11 - (a) AFM topography overview image of a typical graphene-talc device. The white dashed lines delimitate the graphene flake and the scale bar represents 2 μm. (b) Broadband IR near field image with dielectric contrast of Au contact atop of Talc/Au and graphene-Talc interface. (c) SINS point-spectra of the talc/Au (red curve) and graphene-talc/Au (blue curve). The spectra are dominated by the phonon polaritons activity of talc (ν_2 and ν_3) and are modified due to the presence of graphene. (d) Resistance as a function of back-gate voltage (V_G) at room temperature and under N_2 atmosphere for a source-drain voltage of 1 mV. (e) SINS point-spectra for the graphene-talc/Au heterostructure for selected gate bias, demonstrating the gate tunability of the plasmon-phonon polaritons coupling between graphene and talc. (f) Hybridization of graphene plasmons and talc phonons: calculated dispersion relations for graphene-talc system for weakly (left panel, n = 1×10^{10} cm^{-2}) and moderate (right panel, n = 6.5×10^{12} cm^{-2}) doped graphene. The vertical dotted line indicates the momentum excited in by the SINS system due to the AFM tip radius. Copyright 2018: The American Chemical Society.

6. Far-IR polaritons in vdW structures

The examples discussed thus far have involved measurements primarily performed in the mid-IR range, despite the significance of many fundamental excitations and collective modes that have characteristic energies in the far-IR, including the free carrier Drude response, crystal lattice vibrations, charge density waves, superconducting energy gaps, magnetic excitations, and surface plasmon and phonon polaritons. Unlike many laser sources that have a limited tuning range or spectral bandwidth, synchrotron infrared radiation is broadband and extends from the near-infrared into the far-infrared region of the spectrum, making it a unique source for nanospectroscopic measurements. The scarcity of examples in the far-IR arises not from source limitations, but because of the lack of far-infrared detectors with the necessary speed, sensitivity and spectral range. Standard $Hg_{1-x}Cd_xTe$ (MCT) mid-IR detectors can be doped to extend the spectral range below typical values of 600 cm^{-1}, but the extension to lower frequencies comes at the expense of drastically reduced sensitivity. Conventional far-field far-IR detectors, such as pyroelectric deuterated triglycine sulfate (DTGS) detectors or liquid helium cooled Si bolometers, only operate at < few kHz frequencies and have response times too slow to respond to AFM tip tapping frequency (typically ~250 kHz) or to any higher harmonics. There are a few liquid helium cooled detectors, however, that have been used successfully in the far-IR region for s-SNOM and SINS, including Ge:Cu (330 -2000cm^{-1}), Ge:Ga (200-400 cm^{-1}), InSb (40-200 cm^{-1}), and super-conducting bolometers.[128,129]

SINS has been used to directly probe weak excitations in layered materials, including the van der Waals material MoS_2, with its A_{2u} out-of-plane mode at 468 cm^{-1} and E_{1u} in-plane mode at 384 cm^{-1}.[128] Despite the small interlayer coupling, the phonon features show unique symmetry sensitivity even down to 7 nm thickness. SINS has also been used to probe the full voltage-dependent plasmonic response in a pristine monolayer graphene flake[128], similar to previous monochromatic laser IR s-SNOM studies.[30,130] In this case, however, the use of far-IR SINS enabled the direct visualization of the coupled plasmon-phonon interaction in graphene and SiO_2 covering multiple SiO_2 phonon resonances over a spectral range 4 times as large as previous s-SNOM measurements.

Figure 12a shows a significant modulation of the far-IR SINS amplitude and phase signals of the graphene/SiO_2 device upon electrostatic tuning of the back gate voltage V_{GS}. This is consistent with gate tuning of the Drude free carrier response superimposed with the SPP absorption in graphene, as well as the hybridization and strong coupling between the graphene SPPs and the SiO_2 substrate surface phonons. Figure 12b-c also displays the spectral structure of the SINS response within 300 nm of the graphene/SiO_2 interface, which arises from the interference of SPP waves that are launched radially by the metallic probe tip and reflected by the graphene/SiO_2 edge. The SPP dispersion as a function of frequency can readily be observed near the graphene interface, with the polariton wavelength determined by the distance of the modulated near-field amplitude and phase from the edge.

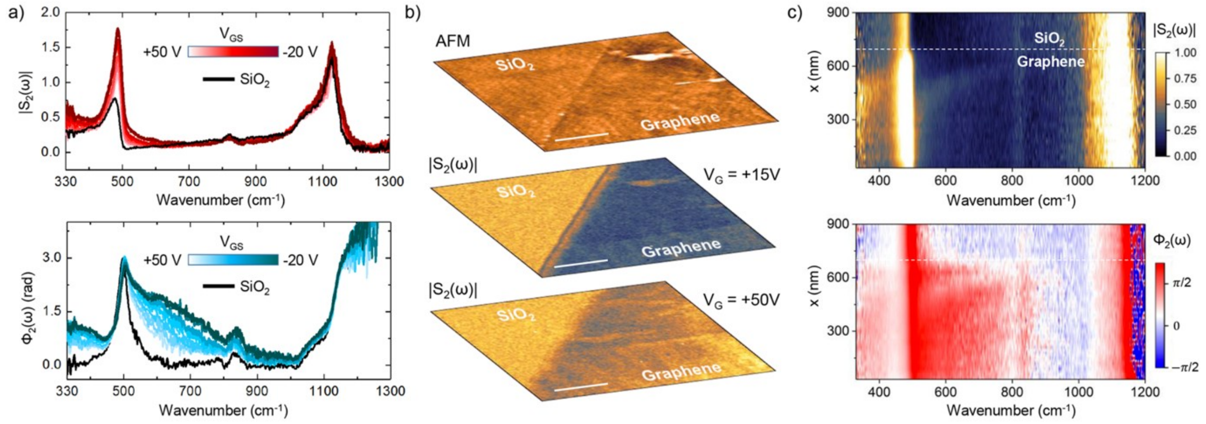

Figure 12 - Far-IR graphene plasmonics. (a) Gate-tuning of SINS amplitude $|S_2(\omega)|$ (red shaded curves) and phase $\Phi_2(\omega)$ (blue shaded curves) for a functional graphene device on SiO_2 (black line), showing modulation of free carrier Drude response and plasmon absorption in graphene. (b) SINS nanoimaging of graphene/SiO_2 interface for highly doped (V_{GS} = +15 V, middle panel) and low-doped (V_{GS} = +50 V, bottom panel) graphene. Scale bar is 1 µm. (c) SINS spatio-spectral linescan across doped-graphene/SiO_2 boundary, demonstrating nanometer broadband spectroscopic access to far-IR surface plasmon polariton (SPP) waves in graphene down to 320 cm^{-1}. The SPP dispersion as a function of energy can be observed directly near the graphene edge, where reflected surface waves constructively interfere with those launched from the AFM tip. Copyright 2018: The American Chemical Society.

7. Summary and Outlook

SINS is an advanced configuration of s-SNOM where synchrotron radiation is used as the far-field excitation. Although broadband IR laser sources are in fast development, synchrotron IR ports are still the only sources with high spectral irradiance across the whole IR spectrum (far, mid and near-IR) with proper repetition rate for s-SNOM. The vast spectral coverage of SINS perfectly suits investigations where multiple dielectric resonances of a material must be monitored in a single acquisition experiment. Additionally, the reduced noise of synchrotrons enables enhanced optical sensitivity for the s-SNOM with low power illumination, allowing long integration times with no risks of radiation damage to the samples. In the theme of 2D and vdW materials, those attributes make SINS an ideal tool for studying the multispectral polaritonic response of these compounds, especially in the cases involving precise lineshape analysis and rigorous intensity comparison of multiple dipolar resonances.

This review paper features an update on how SINS has approached the polaritonic properties of vdW crystals starting with a brief introduction on the physics of polaritons, followed by a description of the SINS experimental scheme and data processing. The paper also highlights the main SINS contributions to the study of hybrid polaritonic activity in graphene-hBN systems,[18][18,66,76] polariton-assisted mapping of local strain in hBN crystals[92] and plasmonic phenomena in metal oxide conductors[100] and vdW semiconductors.[116] The SINS analysis of talc crystals and graphene-talc devices is reviewed and highlights the photonic tunability of this new vdW material.[117] Finally, a demonstration of the extreme spectral reach of SINS to probe the far-IR plasmonics of graphene is revisited, exploiting the long wavelengths sensitivity of a Ge:Cu detector. In this case, continuous nanoscale-resolved spectroscopy from the mid- to the far-IR range (10 µm to 30 µm) was achieved for the first time.[128]

It is relevant to note that a multitude of new polaritonic phenomena in vdW structures has recently been predicted, including in-plane negative refraction,[131] directional excitation,[132] the observation of the inverse Doppler effect[133] and multifrequency superscattering.[134] The experimental observation of these phenomena will require IR spatio-spectral methods, with SINS linescans and hyperspectral imaging consisting of suitable and robust candidates. Furthermore, recent developments in accelerators technology are taking synchrotrons storage rings to a new level in terms of spectral irradiance and beam stability.

These new sources, named 4th generation synchrotrons, have ultimately small emittances (source size versus beam divergence) and are becoming diffraction limited in the energy range of hard X-rays.[135–137] Hence, the current trend for synchrotron experimental stations is to operate with intricate parameter spaces involving beams with large transverse coherence, nanoscale probes, time-resolved experiments, multi-spectral sensitivity and advanced sample environments. In the near-IR to far-IR ranges, the high stability in the emission provided by this new class of synchrotron sources can potentially improve the signal-to-noise ratio of IR-based analytical techniques by a few orders of magnitude. In addition, far-IR detector technology is now evolving to operate with bandwidths compatible to the natural mechanical frequencies of AFM tips used in s-SNOM (few hundreds of kHz). Therefore, the era of long wavelengths synchrotron nanospectroscopy, in a range not fully accessible to current lasers, is just beginning.

8. Acknowledgements

The authors thank Brazilian Synchrotron Light Laboratory (LNLS), Advanced Light Source (ALS) and Metrology Light Source (MLS-PTB) for motivating the Infrared Nanospectroscopy programs in these facilities. IB, FM and RF acknowledge Thiago M. for technical assistance in the experiments performed at the IR beamline of LNLS. This research used resources of the Advanced Light Source, which is a DOE Office of Science User Facility under contract no. DE-AC02-05CH11231.IB acknowledge the financial support from the Brazilian Nanocarbon Institute of Science and Technology (INCT/Nanocarbono). CdM and DAB acknowledge the financial support from the São Paulo Research Foundation (process nos. 2012/50259-8, 2015/11779-4 and 2018/07276-5), CAPES – PRINT (Programa Institucional de Internacionalização; Grant # 88887.310281/2018-00), the Brazilian Nanocarbon Institute of Science and Technology (INCT/Nanocarbono), Fapemig and CNPq. BK gratefully acknowledges the support by the European Metrology Programme for

Innovation and Research (EMPIR) within the framework of the ADVENT project. RF acknowledges the support by CNPq through the research grant 311564/2018-6. The EMPIR initiative is co-funded by the European's Horizon 2020 research and innovation programme and the EMPIR Participating States.

Received: ((will be filled in by the editorial staff))
Revised: ((will be filled in by the editorial staff))

References

[1] D. L. Mills, E. Burstein, V. Gunawan, *Reports Prog. Phys.* **1974**, *37*, 817.

[2] T. Low, A. Chaves, J. D. Caldwell, A. Kumar, N. X. Fang, P. Avouris, T. F. Heinz, F. Guinea, L. Martin-Moreno, F. Koppens, *Nat. Mater.* **2017**, *16*, 182.

[3] D. N. Basov, M. M. Fogler, F. J. Garcia de Abajo, *Science (80-.).* **2016**, *354*, aag1992.

[4] A. K. Geim, I. V Grigorieva, *Nature* **2013**, *499*, 419.

[5] K. S. Novoselov, A. Mishchenko, A. Carvalho, A. H. Castro Neto, *Science (80-.).* **2016**, *353*, DOI 10.1126/science.aac9439.

[6] D. L. Duong, S. J. Yun, Y. H. Lee, *ACS Nano* **2017**, *11*, 11803.

[7] D. Jariwala, T. J. Marks, M. C. Hersam, *Nat. Mater.* **2017**, *16*, 170.

[8] K. S. Novoselov, A. H. Castro Neto, *Phys. Scr.* **2012**, DOI 10.1088/0031-8949/2012/T146/014006.

[9] F. Xia, H. Wang, D. Xiao, M. Dubey, A. Ramasubramaniam, *Nat. Photonics* **2014**, *8*, 899.

[10] F. Hu, Y. Luan, M. E. Scott, J. Yan, D. G. Mandrus, X. Xu, Z. Fei, *Nat. Photonics* **2017**, *11*, 356.

[11] M. Mrejen, L. Yadgarov, A. Levanon, H. Suchowski, *Sci. Adv.* **2019**, *5*, 1.

[12] X. Chen, D. Hu, R. Mescall, G. You, D. N. Basov, Q. Dai, M. Liu, *Adv. Mater.* **2019**, *31*, 1.

[13] Z. Fei, a. S. Rodin, G. O. Andreev, W. Bao, a. S. McLeod, M. Wagner, L. M. Zhang, Z. Zhao, M. Thiemens, G. Dominguez, M. M. Fogler, a. H. C. Neto, C. N. Lau, F. Keilmann, D. N. Basov, *Nature* **2012**, *487*, 82.

[14] J. Chen, M. Badioli, P. Alonso-González, S. Thongrattanasiri, F. Huth, J. Osmond, M. Spasenović, A. Centeno, A. Pesquera, P. Godignon, A. Zurutuza Elorza, N. Camara, F. J. G. G. de Abajo, R. Hillenbrand, F. H. L. Koppens, P. Alonso-Gonzalez, S. Thongrattanasiri, F. Huth, J. Osmond, M. Spasenovic, A. Centeno, A. Pesquera, P. Godignon, A. Zurutuza Elorza, N. Camara, F. J. G. G. de Abajo, R. Hillenbrand, F. H. L. Koppens, A. Z. Elorza, N. Camara, F. J. García de Abajo, R. Hillenbrand, F. H. L. Koppens, *Nature* **2012**, *487*, 77.

[15] S. Dai, Z. Fei, Q. Ma, A. S. Rodin, M. Wagner, A. S. McLeod, M. K. Liu, W. Gannett, W. Regan, K. Watanabe, T. Taniguchi, M. Thiemens, G. Dominguez, A. H. C. Neto, A. Zettl, F. Keilmann, P. Jarillo-Herrero, M. M. Fogler, D. N. Basov, *Science (80-.).* **2014**, *343*, 1125.

[16] W. Ma, P. Alonso-González, S. Li, A. Y. Nikitin, J. Yuan, J. Martín-Sánchez, J. Taboada-Gutiérrez, I. Amenabar, P. Li, S. Vélez, C. Tollan, Z. Dai, Y. Zhang, S. Sriram, K. Kalantar-Zadeh, S. T. Lee, R. Hillenbrand, Q. Bao, *Nature* **2018**, *562*, 557.

[17] S. Dai, Q. Ma, M. K. Liu, T. Andersen, Z. Fei, M. D. Goldflam, M. Wagner, K. Watanabe, T. Taniguchi, M. Thiemens, F. Keilmann, G. C. A. M. A. M. Janssen, S.-E. E. Zhu, P. Jarillo-Herrero, M. M. Fogler, D. N. Basov, *Nat. Nanotechnol.* **2015**, *10*, 682.

[18] F. C. B. Maia, B. T. O'Callahan, A. R. Cadore, I. D. Barcelos, L. C. Campos, K. Watanabe, T. Taniguchi, C. Deneke, A. Belyanin, M. B. Raschke, R. O. Freitas, *Nano Lett.* **2019**, *19*, 708.

[19] F. Zenhausern, Y. Martin, H. K. Wickramasinghe, *Science* **1995**, *269*, 1083.

[20] B. Knoll, F. Keilmann, *Nature* **1999**, *399*, 7.

[21] S. Kawata, Y. Inouye, *Ultramicroscopy* **1995**, *57*, 313.

[22] F. Keilmann, R. Hillenbrand, *Philos. Trans. A. Math. Phys. Eng. Sci.* **2004**, *362*, 787.

[23] P. Hermann, A. Hoehl, P. Patoka, F. Huth, E. Rühl, G. Ulm, *Opt. Express* **2013**, *21*, 2913.

[24] H. A. Bechtel, E. A. Muller, R. L. Olmon, M. C. Martin, M. B. Raschke, *Proc. Natl. Acad. Sci.* **2014**, *111*, 7191.

[25] R. O. Freitas, C. Deneke, F. C. B. Maia, H. G. Medeiros, T. Moreno, P. Dumas, Y. Petroff, H. Westfahl, *Opt. Express* **2018**, *26*, 11238.

[26] A. Ambrosio, M. Tamagnone, K. Chaudhary, L. A. Jauregui, P. Kim, W.

L. Wilson, F. Capasso, *Light Sci. Appl.* **2018**, *7*, DOI 10.1038/s41377-018-0039-4.

[27] Z. Fei, G. O. Andreev, W. Bao, L. M. Zhang, A. S. McLeod, C. Wang, M. K. Stewart, Z. Zhao, G. Dominguez, M. Thiemens, M. M. Fogler, M. J. Tauber, A. H. Castro-Neto, C. N. Lau, F. Keilmann, D. N. Basov, *Nano Lett.* **2011**, *11*, 4701.

[28] P. A. D. Gonçalves, N. M. R. Peres, *An Introduction to Graphene Plasmonics*, WORLD SCIENTIFIC, **2016**.

[29] N. Rivera, T. Christensen, P. Narang, *Nano Lett.* **2019**, *19*, 2653.

[30] Z. Fei, A. S. Rodin, G. O. Andreev, W. Bao, A. S. McLeod, M. Wagner, L. M. Zhang, Z. Zhao, M. Thiemens, G. Dominguez, M. M. Fogler, A. H. C. Neto, C. N. Lau, F. Keilmann, D. N. Basov, *Nature* **2012**, *487*, 82.

[31] J. Chen, M. Badioli, P. Alonso-González, S. Thongrattanasiri, F. Huth, J. Osmond, M. Spasenović, A. Centeno, A. Pesquera, P. Godignon, A. Z. Elorza, N. Camara, F. J. García de Abajo, R. Hillenbrand, F. H. L. Koppens, *Nature* **2012**, *487*, 77.

[32] G. X. Ni, A. S. McLeod, Z. Sun, L. Wang, L. Xiong, K. W. Post, S. S. Sunku, B.-Y. Jiang, J. Hone, C. R. Dean, M. M. Fogler, D. N. Basov, *Nature* **2018**, *557*, 530.

[33] J. A. Gerber, S. Berweger, B. T. O'Callahan, M. B. Raschke, *Phys. Rev. Lett.* **2014**, *113*, 1.

[34] E. Ungersboeck, S. Dhar, G. Karlowatz, V. Sverdlov, H. Kosina, S. Selberherr, *IEEE Trans. Electron Devices* **2007**, *54*, 2183.

[35] B. Kästner, C. M. Johnson, P. Hermann, M. Kruskopf, K. Pierz, A.

Hoehl, A. Hornemann, G. Ulrich, J. Fehmel, P. Patoka, E. Rühl, G. Ulm, *ACS Omega* **2018**, *3*, 4141.

[36] J. D. Caldwell, I. Aharonovich, G. Cassabois, J. H. Edgar, B. Gil, D. N. Basov, *Nat. Rev. Mater.* **2019**, *4*, 552.

[37] T. Low, A. Chaves, J. D. Caldwell, A. Kumar, N. X. Fang, P. Avouris, T. F. Heinz, F. Guinea, L. Martin-Moreno, F. Koppens, **2016**, *16*, DOI 10.1038/nmat4792.

[38] E. E. Narimanov, A. V. Kildishev, *Nat. Photonics* **2015**, *9*, 214.

[39] L. V. Brown, M. Davanco, Z. Sun, A. Kretinin, Y. Chen, J. R. Matson, I. Vurgaftman, N. Sharac, A. J. Giles, M. M. Fogler, T. Taniguchi, K. Watanabe, K. S. Novoselov, S. A. Maier, A. Centrone, J. D. Caldwell, *Nano Lett.* **2018**, *18*, 1628.

[40] M. Tamagnone, A. Ambrosio, K. Chaudhary, L. A. Jauregui, P. Kim, W. L. Wilson, F. Capasso, *Sci. Adv.* **2018**, *4*, 4.

[41] P. Li, M. Lewin, A. V. Kretinin, J. D. Caldwell, K. S. Novoselov, T. Taniguchi, K. Watanabe, F. Gaussmann, T. Taubner, *Nat. Commun.* **2015**, *6*, 7507.

[42] S. Dai, Q. Ma, T. Andersen, A. S. Mcleod, Z. Fei, M. K. Liu, M. Wagner, K. Watanabe, T. Taniguchi, M. Thiemens, F. Keilmann, P. Jarillo-Herrero, M. M. Fogler, D. N. Basov, *Nat. Commun.* **2015**, *6*, 6963.

[43] F. J. Alfaro-Mozaz, P. Alonso-González, S. Vélez, I. Dolado, M. Autore, S. Mastel, F. Casanova, L. E. Hueso, P. Li, A. Y. Nikitin, R. Hillenbrand, & R. Hillenbrand, *Nat. Commun.* **2017**, *8*, 15624.

[44] P. Li, I. Dolado, F. J. Alfaro-Mozaz, F. Casanova, L. E. Hueso, S. Liu, J.

H. Edgar, A. Y. Nikitin, S. Vélez, R. Hillenbrand, *Science (80-.).* **2018**, *359*, 892.

[45] T. U. Tumkur, X. Yang, B. Cerjan, N. J. Halas, P. Nordlander, I. Thomann, *Nano Lett.* **2016**, *16*, 7942.

[46] S. Dai, M. Tymchenko, Y. Yang, Q. Ma, M. Pita-Vidal, K. Watanabe, T. Taniguchi, P. Jarillo-Herrero, M. M. Fogler, A. Alù, D. N. Basov, *Adv. Mater.* **2018**, *30*, 1.

[47] J. Duan, R. Chen, J. Li, K. Jin, Z. Sun, J. Chen, *Adv. Mater.* **2017**, *1702494*, 1702494.

[48] S. Dai, Q. Ma, Y. Yang, J. Rosenfeld, M. D. Goldflam, A. McLeod, Z. Sun, T. I. Andersen, Z. Fei, M. Liu, Y. Shao, K. Watanabe, T. Taniguchi, M. Thiemens, F. Keilmann, P. Jarillo-Herrero, M. M. Fogler, D. N. Basov, *Nano Lett.* **2017**, *17*, 5285.

[49] E. Yoxall, M. Schnell, A. Y. Nikitin, O. Txoperena, A. Woessner, M. B. Lundeberg, F. Casanova, L. E. Hueso, F. H. L. Koppens, R. Hillenbrand, *Nat. Photonics* **2015**, *9*, 674.

[50] I. D. Barcelos, A. R. Cadore, L. C. Campos, A. Malachias, K. Watanabe, T. Taniguchi, F. C. B. Maia, R. Freitas, C. Deneke, *Nanoscale* **2015**, *7*, 11620.

[51] S. Dai, Q. Ma, M. K. Liu, T. Andersen, Z. Fei, M. D. Goldflam, M. Wagner, K. Watanabe, T. Taniguchi, M. Thiemens, F. Keilmann, G. C. A. M. Janssen, S.-E. Zhu, P. Jarillo-Herrero, M. M. Fogler, D. N. Basov, *Nat. Nanotechnol.* **2015**, *10*, 682.

[52] A. V Shchegrov, K. Joulain, R. Carminati, J.-J. Greffet, *Phys. Rev. Lett.*

2000, *85*, 1548.

[53] R. Hillenbrand, T. Taubner, F. Keilmann, *Nature* **2002**, *418*, 159.

[54] S. Amarie, F. Keilmann, *Phys. Rev. B - Condens. Matter Mater. Phys.* **2011**, *83*, 1.

[55] L. M. Zhang, G. O. Andreev, Z. Fei, A. S. McLeod, G. Dominguez, M. Thiemens, A. H. Castro-Neto, D. N. Basov, M. M. Fogler, *Phys. Rev. B* **2012**, *85*, 75419.

[56] P. Alonso-Gonzalez, a Y. Nikitin, F. Golmar, A. Centeno, A. Pesquera, S. Velez, J. Chen, G. Navickaite, F. Koppens, A. Zurutuza, F. Casanova, L. E. Hueso, R. Hillenbrand, *Science (80-.).* **2014**, *344*, 1.

[57] P. Li, M. Lewin, A. V Kretinin, J. D. Caldwell, K. S. Novoselov, T. Taniguchi, K. Watanabe, F. Gaussmann, T. Taubner, *Nat. Commun.* **2015**, *6*, 7507.

[58] A. Woessner, M. B. Lundeberg, Y. Gao, A. Principi, P. Alonso-González, M. Carrega, K. Watanabe, T. Taniguchi, G. Vignale, M. Polini, J. Hone, R. Hillenbrand, F. H. L. Koppens, *Nat. Mater. 14*, 421.

[59] G. X. Ni, L. Wang, M. D. Goldflam, M. Wagner, Z. Fei, A. S. McLeod, M. K. Liu, F. Keilmann, B. Özyilmaz, A. H. Castro Neto, J. Hone, M. M. Fogler, D. N. Basov, *Nat. Photonics* **2016**, *10*, 244.

[60] A. Y. Nikitin, P. Alonso-González, S. Vélez, S. Mastel, A. Centeno, A. Pesquera, A. Zurutuza, F. Casanova, L. E. Hueso, F. H. L. Koppens, R. Hillenbrand, *Nat. Photonics* **2016**, *10*, 239.

[61] P. Li, X. Yang, T. W. W. Maß, J. Hanss, M. Lewin, A.-K. U. Michel, M. Wuttig, T. Taubner, *Nat. Mater.* **2016**, *15*, 870.

[62] M. B. Lundeberg, Y. Gao, A. Woessner, C. Tan, P. Alonso-González, K. Watanabe, T. Taniguchi, J. Hone, R. Hillenbrand, F. H. L. Koppens, *Nat. Mater.* **2016**, *1*, doi:10.1038/nmat4755.

[63] P. Alonso-González, A. Y. Nikitin, Y. Gao, A. Woessner, M. B. Lundeberg, A. Principi, N. Forcellini, W. Yan, S. Vélez, A. J. Huber, K. Watanabe, T. Taniguchi, F. Casanova, L. E. Hueso, M. Polini, J. Hone, F. H. L. Koppens, R. Hillenbrand, *Nat. Nanotechnol.* **2017**, *12*, 31.

[64] Z. Fei, J. J. Foley, W. Gannett, M. K. Liu, S. Dai, G. X. Ni, A. Zettl, M. M. Fogler, G. P. Wiederrecht, S. K. Gray, D. N. Basov, *Nano Lett.* **2016**, acs. nanolett.6b04076.

[65] L. Ju, B. Geng, J. Horng, C. Girit, M. Martin, Z. Hao, H. a Bechtel, X. Liang, A. Zettl, Y. R. Shen, F. Wang, *Nat. Nanotechnol.* **2011**, *6*, 630.

[66] I. D. Barcelos, A. R. Cadore, L. C. Campos, A. Malachias, K. Watanabe, T. Taniguchi, F. Barbosa Maia, R. D. O. Freitas, C. Deneke, F. C. B. Maia, R. D. O. Freitas, C. Deneke, *Nanoscale* **2015**, *7*, 11620.

[67] Z. Fei, a S. Rodin, W. Gannett, S. Dai, W. Regan, M. Wagner, M. K. Liu, a S. McLeod, G. Dominguez, M. Thiemens, A. H. Castro Neto, F. Keilmann, A. Zettl, R. Hillenbrand, M. M. Fogler, D. N. Basov, *Nat. Nanotechnol.* **2013**, *8*, 821.

[68] F. Huth, M. Schnell, J. Wittborn, N. Ocelic, R. Hillenbrand, *Nat. Mater.* **2011**, *10*, 352.

[69] F. Huth, A. Govyadinov, S. Amarie, W. Nuansing, F. Keilmann, R. Hillenbrand, *Nano Lett.* **2012**, *12*, 3973.

[70] P. Hermann, A. Hoehl, G. Ulrich, C. Fleischmann, A. Hermelink, B.

Kästner, P. Patoka, A. Hornemann, B. Beckhoff, E. Rühl, G. Ulm, *Opt. Express* **2014**, *22*, 17948.

[71] B. Pollard, F. C. B. Maia, M. B. Raschke, R. O. Freitas, *Nano Lett.* **2016**, *16*, 55.

[72] W. D. Duncan, G. P. Williams, B. Hill, B. National, *Appl. Opt.* **1983**, *22*.

[73] L. Y. and Y. W. Jianlei Cui, *Laser Phys.* **2013**, *23*, 076003.

[74] R. Hillenbrand, F. Keilmann, *Phys. Rev. Lett.* **2000**, *85*, 3029.

[75] P. R. Griffiths, J. A. de Haseth, *Fourier Transform Infrared Spectrometry*, John Wiley & Sons, Inc., Hoboken, NJ, USA, **2007**.

[76] Z. Shi, H. A. Bechtel, S. Berweger, Y. Sun, B. Zeng, C. Jin, H. Chang, M. C. Martin, M. B. Raschke, F. Wang, *ACS Photonics* **2015**, *2*, 790.

[77] G. G. Naumis, S. Barraza-Lopez, M. Oliva-Leyva, H. Terrones, *Reports Prog. Phys.* **2017**, *80*, 96501.

[78] F. Guinea, *Solid State Commun.* **2012**, *152*, 1437.

[79] Welser, Hoyt, Gibbons, in *1992 Int. Tech. Dig. Electron Devices Meet.*, **1992**, pp. 1000–1002.

[80] J. Welser, J. L. Hoyt, J. F. Gibbons, *IEEE Electron Device Lett.* **1994**, *15*, 100.

[81] K. Uchida, T. Krishnamohan, K. C. Saraswat, Y. Nishi, in *IEEE Int. Devices Meet. 2005. IEDM Tech. Dig.*, **2005**, pp. 129–132.

[82] C. Lee, X. Wei, J. W. Kysar, J. Hone, **2008**, *321*, 385.

[83] F. Guinea, M. I. Katsnelson, A. K. Geim, *Nat. Phys.* **2009**, *6*, 30.

[84] N. Levy, S. A. Burke, K. L. Meaker, M. Panlasigui, A. Zettl, F. Guinea, A. H. C. Neto, M. F. Crommie, *Science (80-.).* **2010**, *329*, 544 LP.

[85] Y. Jiang, J. Mao, J. Duan, X. Lai, K. Watanabe, T. Taniguchi, E. Y. Andrei, *Nano Lett.* **2017**, *17*, 2839.

[86] V. M. Pereira, A. H. Castro Neto, *Phys. Rev. Lett.* **2009**, *103*, 046801.

[87] A. Castellanos-Gomez, R. Roldán, E. Cappelluti, M. Buscema, F. Guinea, H. S. J. van der Zant, G. A. Steele, *Nano Lett.* **2013**, *13*, 5361.

[88] A. Falin, Q. Cai, E. J. G. Santos, D. Scullion, D. Qian, R. Zhang, Z. Yang, S. Huang, K. Watanabe, T. Taniguchi, M. R. Barnett, Y. Chen, R. S. Ruoff, L. H. Li, *Nat. Commun.* **2017**, *8*, 15815.

[89] J. Wang, F. Ma, M. Sun, *RSC Adv.* **2017**, *7*, 16801.

[90] C. Androulidakis, E. N. Koukaras, M. Poss, K. Papagelis, C. Galiotis, S. Tawfick, *Phys. Rev. B* **2018**, *97*, 241414.

[91] A. J. Huber, A. Ziegler, T. Köck, R. Hillenbrand, *Nat. Nanotechnol.* **2009**, *4*, 153.

[92] B. Lyu, H. Li, L. Jiang, W. Shan, C. Hu, A. Deng, Z. Ying, L. Wang, Y. Zhang, H. A. Bechtel, M. C. Martin, T. Taniguchi, K. Watanabe, W. Luo, F. Wang, Z. Shi, *Nano Lett.* **2019**, *19*, 1982.

[93] B. Lyu, H. Li, L. Jiang, W. Shan, C. Hu, A. Deng, Z. Ying, L. Wang, Y. Zhang, H. A. Bechtel, M. C. Martin, T. Taniguchi, K. Watanabe, W. Luo, F. Wang, Z. Shi, *Nano Lett.* **2019**, DOI 10.1021/acs.nanolett.8b05166.

[94] J. Kim, A. Dutta, G. V. Naik, A. J. Giles, F. J. Bezares, C. T. Ellis, J. G. Tischler, A. M. Mahmoud, H. Caglayan, O. J. Glembocki, A. V. Kildishev, J. D. Caldwell, A. Boltasseva, N. Engheta, *Optica* **2016**, *3*, 339.

[95] M. Z. Alam, I. De Leon, R. W. Boyd, *Science (80-.).* **2016**, *352*, 795.

[96] S. D. Lounis, E. L. Runnerstrom, A. Llordés, D. J. Milliron, *J. Phys. Chem. Lett.* **2014**, *5*, 1564.

[97] R. Buonsanti, A. Llordes, S. Aloni, B. A. Helms, D. J. Milliron, *Nano Lett.* **2011**, *11*, 4706.

[98] M. Kanehara, H. Koike, T. Yoshinaga, T. Teranishi, *J. Am. Chem. Soc.* **2009**, *131*, 17736.

[99] X. Ye, J. Fei, B. T. Diroll, T. Paik, C. B. Murray, *J. Am. Chem. Soc.* **2014**, *136*, 11680.

[100] R. W. Johns, H. a Bechtel, E. L. Runnerstrom, A. Agrawal, S. D. Lounis, D. J. Milliron, *Nat. Commun.* **2016**, *7*, 11583.

[101] C. Sönnichsen, T. Franzl, T. Wilk, G. von Plessen, J. Feldmann, O. Wilson, P. Mulvaney, *Phys. Rev. Lett.* **2002**, *88*, 77402.

[102] K. Lindfors, T. Kalkbrenner, P. Stoller, V. Sandoghdar, *Phys. Rev. Lett.* **2004**, *93*, 37401.

[103] O. L. Muskens, N. Del Fatti, F. ValÍe, J. R. Huntzinger, P. Billaud, M. Broyer, *Appl. Phys. Lett.* **2006**, *88*, 14.

[104] J. A. Wilson, A. D. Yoffe, *Adv. Phys.* **1969**, *18*, 193.

[105] A. Splendiani, L. Sun, Y. Zhang, T. Li, J. Kim, C.-Y. Chim, G. Galli, F. Wang, *Nano Lett.* **2010**, *10*, 1271.

[106] K. F. Mak, K. He, J. Shan, T. F. Heinz, *Nat. Nanotechnol.* **2012**, *7*, 494.

[107] A. N. Grigorenko, M. Polini, K. S. Novoselov, *Nat. Photonics* **2012**, *6*, 749.

[108] T. Low, P. Avouris, *ACS Nano* **2014**, *8*, 1086.

[109] T. Stauber, *J. Phys. Condens. Matter* **2014**, *26*, 123201.

[110] A. Scholz, T. Stauber, J. Schliemann, *Phys. Rev. B* **2013**, *88*, 35135.

[111] K. M. Goodfellow, R. Beams, C. Chakraborty, L. Novotny, A. N. Vamivakas, *Optica* **2014**, *1*, 149.

[112] S. Butun, S. Tongay, K. Aydin, *Nano Lett.* **2015**, *15*, 2700.

[113] Y. Lin, X. Ling, L. Yu, S. Huang, A. L. Hsu, Y.-H. Lee, J. Kong, M. S. Dresselhaus, T. Palacios, *Nano Lett.* **2014**, *14*, 5569.

[114] Z. Fei, G. O. Andreev, W. Bao, L. M. Zhang, A. S. McLeod, C. Wang, M. K. Stewart, Z. Zhao, G. Dominguez, M. Thiemens, M. M. Fogler, M. J. Tauber, A. H. Castro-Neto, C. N. Lau, F. Keilmann, D. N. Basov, *Nano Lett.* **2011**, *11*, 4701.

[115] P. Patoka, G. Ulrich, A. E. Nguyen, L. Bartels, P. A. Dowben, V. Turkowski, T. S. Rahman, P. Hermann, B. Kästner, A. Hoehl, G. Ulm, E. Rühl, *Opt. Express* **2016**, *24*, 4600.

[116] P. Patoka, G. Ulrich, A. E. Nguyen, L. Bartels, P. A. Dowben, V. Turkowski, T. S. Rahman, P. Hermann, B. Kästner, G. Ulm, E. Rühl, *Opt. Express* **2016**, *24*, 1154.

[117] I. D. Barcelos, A. R. Cadore, A. B. Alencar, F. C. B. Maia, E. Mania, R. F. Oliveira, C. C. B. Bufon, Â. Malachias, R. O. Freitas, R. L. Moreira, H. Chacham, *ACS Photonics* **2018**, *5*, 1912.

[118] Q. Bao, K. P. Loh, *ACS Nano* **2012**, *6*, 3677.

[119] A. Politano, G. Chiarello, *Nanoscale* **2014**, *6*, 10927.

[120] S. Xiao, X. Zhu, B.-H. Li, N. A. Mortensen, *Front. Phys.* **2016**, *11*, 117801.

[121] A. B. Alencar, A. P. M. Barboza, B. S. Archanjo, H. Chacham, B. R. A. Neves, *2D Mater.* **2015**, *2*, 015004.

[122] E. Mania, A. B. Alencar, A. R. Cadore, B. R. Carvalho, K. Watanabe, T. Taniguchi, B. R. A. Neves, H. Chacham, L. C. Campos, *2D Mater.* **2017**, *4*, 031008.

[123] A. R. Cadore, E. Mania, A. B. Alencar, N. P. Rezende, S. de Oliveira, K. Watanabe, T. Taniguchi, H. Chacham, L. C. Campos, R. G. Lacerda, *Sensors Actuators B Chem.* **2018**, *266*, 438.

[124] R. W. . Wilkins, J. Ito, *Am. Mineral.* **1967**, *52*, 1649.

[125] V. C. Farmer, *Mineral. Mag.* **1958**, *21*, 829.

[126] G. Ulian, G. Valdrè, *Phys. Chem. Miner.* **2014**, *42*, 151.

[127] A. B. Alencar, A. P. M. Barboza, B. S. Archanjo, H. Chacham, B. R. A. Neves, *2D Mater.* **2015**, *2*, 015004.

[128] O. Khatib, H. A. Bechtel, M. C. Martin, M. B. Raschke, G. L. Carr, *ACS Photonics* **2018**, *5*, 2773.

[129] D. Lang, J. Döring, T. Nörenberg, Á. Butykai, I. Kézsmárki, H. Schneider, S. Winnerl, M. Helm, S. C. Kehr, L. M. Eng, *Rev. Sci. Instrum.* **2018**, *89*, DOI 10.1063/1.5016281.

[130] J. Chen, M. Badioli, P. Alonso-González, S. Thongrattanasiri, F. Huth, J. Osmond, M. Spasenović, A. Centeno, A. Pesquera, P. Godignon, A. Zurutuza Elorza, N. Camara, F. J. G. G. de Abajo, R. Hillenbrand, F. H. L. Koppens, P. Alonso-Gonzalez, S. Thongrattanasiri, F. Huth, J. Osmond, M. Spasenovic, A. Centeno, A. Pesquera, P. Godignon, A. Zurutuza Elorza, N. Camara, F. J. G. G. de Abajo, R. Hillenbrand, F. H.

L. Koppens, *Nature* **2012**, *advance on*, 1.

[131] X. Lin, Y. Yang, N. Rivera, J. J. López, Y. Shen, I. Kaminer, H. Chen, B. Zhang, J. D. Joannopoulos, M. Soljačic, *Proc. Natl. Acad. Sci. U. S. A.* **2017**, *114*, 6717.

[132] Y. Jiang, X. Lin, T. Low, B. Zhang, H. Chen, *Laser Photonics Rev.* **2018**, *12*, 10.

[133] X. Shi, X. Lin, I. Kaminer, F. Gao, Z. Yang, J. D. Joannopoulos, M. Soljačić, B. Zhang, *Nat. Phys.* **2018**, *14*, 1001.

[134] C. Qian, X. Lin, Y. Yang, F. Gao, Y. Shen, J. Lopez, I. Kaminer, B. Zhang, E. Li, M. Soljačić, H. Chen, *ACS Photonics* **2018**, *5*, 1506.

[135] E. Samuel Reich, *Nature* **2013**, *501*, 148.

[136] M. M. Waldrop, *Nature* **2014**, *505*, 604.

[137] D. Castelvecchi, *Nature* **2015**, *525*, 15.